Investigating High-Velocity Stars Ejected from the Cores of Globular Clusters

by

Abigail Battson

A THESIS SUBMITTED IN PARTIAL FULFILMENT OF
THE REQUIREMENTS FOR THE DEGREE OF

BACHELOR OF SCIENCE

in

Honours Astrophysics

(Department of Astronomy and Physics, Dr. Vincent Hénault-Brunet supervising faculty)

.....

.....

.....

.....

.....

SAINT MARY'S UNIVERSITY

April 22, 2023

Abstract

Investigating High-Velocity Stars Ejected from the Cores of Globular Clusters

by *Abigail Battson*

submitted on April 22, 2023:

The dense environment in the cores of globular clusters enables three-body interactions involving a binary system and a single star to occur frequently, which can eject high-velocity stars from the cluster. The velocities of these stars reflect the masses involved in the interactions which accelerated them, making them promising tracers of stellar remnants in globular clusters, particularly the black hole population. We use *Gaia* Data Release 3 data to locate high-velocity stars in the regions around a large number of Milky Way globular clusters, finding over 2000 candidates for 53 of the investigated clusters. Thirteen of these clusters are selected for further analysis in order to determine the potential origins of the observed high-velocity stars. The velocity distribution of the ejected high-velocity stars is predicted analytically and compared to the observed samples for a number of scenarios of different three-body interactions, mostly involving compact objects such as black holes. We can determine that the likely object which has been involved in the interaction that produced these stars must be a black hole for some cases. We

have found evidence of the presence of black holes in nine globular clusters. We discuss future directions and improvements to this work which will allow for further constraints on black hole populations within globular clusters.

Contents

List of Figures

List of Tables

Chapter 1

Introduction

1.1 Globular Clusters

In the galactic halo of most galaxies orbit spherical gravitationally bound groups of thousands to millions of stars, known as globular clusters (GCs). These groups of stars are generally formed all at the same time, and are old, type II stars around 10-12 billion years old. These clusters are quite numerous, with over 150 globular clusters known in the Milky Way galaxy (e.g. Harris, 2010). Globular clusters have a dense core, with a decreasing density of stars farther from the cluster core, as seen in the globular cluster NGC 362 in Figure 1.1. The most massive objects within these clusters are stellar remnants (white dwarfs, neutron stars and black holes), binary star systems, and giant stars, with most objects in the cluster being low-mass main sequence stars, since the initial mass function is biased towards low-mass stars and the higher mass stars have lived out their main-sequence lifespan. Binary star systems, systems where two stars orbit each other, are relatively common in globular clusters with approximately 10% of all stars in globular clusters being in binary systems (e.g. Hut et al., 1992). Globular clusters are interesting objects to study for a number of reasons, including the fact that their high densities make them an ideal laboratory to study stellar dynamics and a range of astrophysical phenomena.

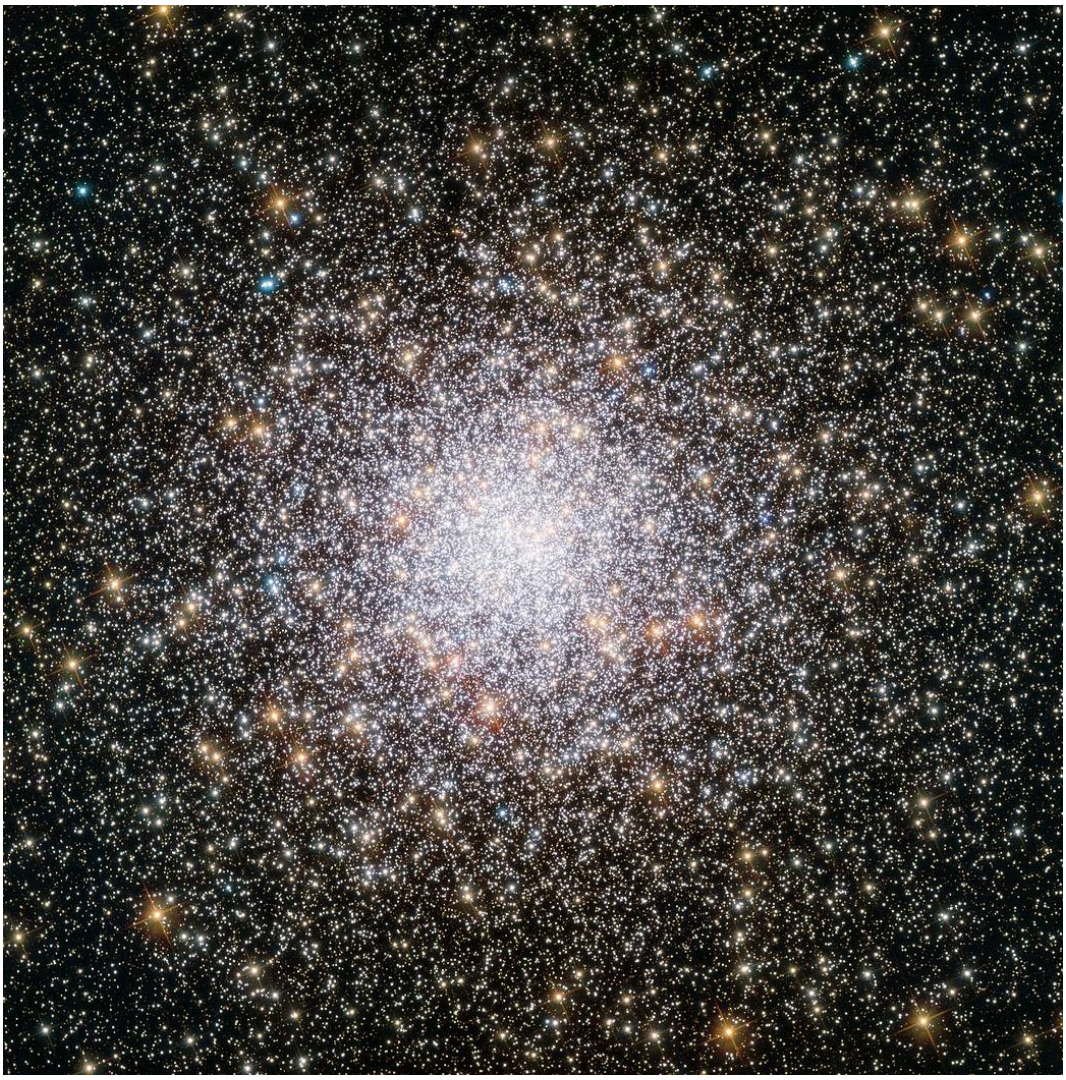

Figure 1.1: A Globular Cluster, NGC 362, pictured by Hubble's Advanced Camera for Surveys. Photo credit to ESA/Hubble & NASA.

1.1.1 Interactions between Stars in Globular Clusters

The highest-mass objects migrate to the core of a globular cluster over time, due to a process known as two-body relaxation and mass segregation, where individual stars or systems of 2 stars interact with one another (e.g. Heggie & Hut, 2003). The higher-mass stars lose speed from these interactions, sinking to the cluster centre while the lower-mass stars tend to migrate outwards. This is due to a tendency towards kinetic

energy equipartition from the effects of two-body encounters. By this process, most of the black holes, neutron stars, white dwarfs and binary stars will lie within the cores of the globular clusters.

In the dense core populated by the highest-mass objects within a globular cluster, gravitational interactions between objects continue to occur which can have important consequences. One of the primary locations where black hole mergers are hypothesized to take place is in these dense cores, where clusters can contain significant numbers of black holes (e.g., Weatherford et al., 2020, 2021; Vitral & Mamon, 2021). Black holes which may exist in the cores of globular clusters can dynamically form binaries with other objects in the cores, including other black holes (e.g., Rodriguez et al., 2019; Antonini et al., 2019). Through a process described in depth in Section 1.2, these binaries will begin to shrink after losing energy during gravitational interactions with other objects. If a binary shrinks sufficiently, it may begin merging, emitting gravitational waves which can be detected using gravitational wave detectors such as the Laser Interferometer Gravitational-wave Observatory, or LIGO (Abbott et al., 2016). This environment may also be a candidate to form more massive black holes known as intermediate mass black holes, which lie in the mass gap between stellar-mass and supermassive black holes, via the mergers of smaller black holes (e.g., Giersz et al., 2015; Mapelli et al., 2021).

1.2 Three-Body Interactions in Globular Clusters

In dense environments, there is a higher rate of close encounters, from not only two single bodies but also binary-star and binary-binary interactions (e.g. Gvaramadze et al., 2009). These interactions result in an exchange of energy between the components, which can take several different forms. Mergers between objects can be a source of gravitational waves, while other interactions can result in the ejection of a star whose velocity depends on the energy and thus mass of the objects involved in its ejection (e.g. Lützgendorf et al., 2012). All objects within a globular cluster have kinetic energy, $E_{kin} = \frac{1}{2}mv^2$, with m being the mass of the object and v being its speed, but binaries have an additional energy reserve known as their internal energy E_{bin}, given by

$$E_{bin} = -\frac{Gm_1m_2}{2a} = -E_b \tag{1.1}$$

(Heggie & Hut, 2003). m_1 and m_2 are the masses of the binary components, a is the binary semi-major axis, and E_b is known as the binding energy, taken as a positive quantity. The behaviour of a binary during an interaction depends on the type of binary it is, either hard or soft. A hard binary is a binary which tends to become more bound upon interaction with another body, while a soft binary is a binary which tends to become less bound during an interaction (e.g. Heggie & Hut, 2003). This can be generalized to give the hard-soft limit $E_b \approx \frac{1}{2}\langle m\rangle\sigma^2$ for the boundary between a hard and soft binary, where if the binding energy of the binary is greater then the

average kinetic energy of the stars (σ is the velocity dispersion of stars in the region, and $\langle m \rangle$ the average mass), it is a hard binary, and vice-versa for a soft binary (Heggie & Hut, 2003).

Primordial binaries, those formed during the early star formation process, will be formed as either hard or soft binaries. Dynamically formed binaries, where one object captures another object to form a binary generally form around the hard-soft limit (e.g. Antonini et al., 2019). Binaries will undergo a large number of three-body interactions over the course of their life, thus losing or gaining binding energy, respectively softening or hardening. A soft binary will eventually become ionized, while a hard binary will harden until a certain point. A hard binary formed at approximately the hard-soft limit will undergo encounters with other objects and become more bound with their final separation a_f being less than the binary's initial separation a_i. This results in a more negative E_{bin}, while the single objects in the three-body interaction, the 'interlopers', will gain some of the energy lost by the binaries in these interactions and the binaries will experience a recoil velocity in the opposite direction. The hardening rate of binaries, $\frac{dE_b}{dt}$ is approximately constant with time (e.g. Antonini et al., 2019). Binaries in globular clusters thus shrink at a constant rate until they reach a limiting semi-major axis. If a binary shrinks to a certain radius, a_{ej}

$$a_{ej} \approx 0.1 \text{ AU}(\frac{m_1 m_2}{m_1+m_2+m_3}\frac{m_3}{m_1+m_2}\frac{0.6}{M_\odot})(\frac{50 \text{ km/s}}{v_{esc}})^2, \tag{1.2}$$

it will be ejected from the cluster, as the binary recoil velocity can exceed the cluster's

escape velocity at this semi-major axis (e.g. Antonini et al., 2019; Antonini & Rasio, 2016). m_1 and m_2 are the binary component masses, m_3 is the mass of the single object, and v_{esc} is the escape velocity of the cluster.

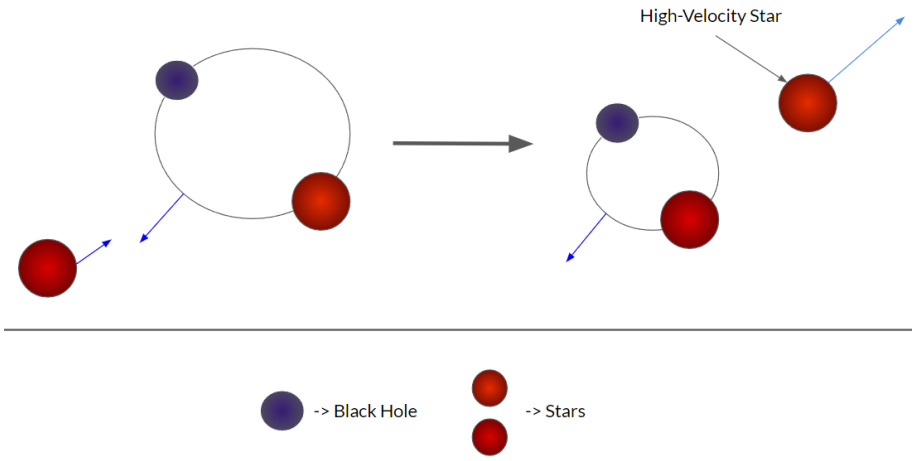

Figure 1.2: A simplified schematic of a 3-body flyby involving two stars and a black hole. The single star gains energy, while the binary hardens.

The type of three-body interaction which causes the shrinking of binaries is a flyby interaction, which simply results in a binary shrinking or growing and the third 'interloper' star gaining or losing energy/velocity. A flyby with a hard binary will further harden the binary, illustrated in Figure 1.2. There are other types of three-body interactions however, which will vary in likelihood depending on the relative masses of the components. One of these is an exchange, which occurs when the interloper star takes the place of one of the binary members, resulting in a new binary, and a new single ejected star (e.g. Lützgendorf et al., 2012). This generally occurs when the single interloper has a greater mass than either of the original stars in the binary. The probability of exchange is a function of the relative mass of the intruder to the binary components. A depiction of how the exchange probability changes

with relative mass of the intruder found using numerical simulations can be seen in Figure 1.3. These simulated encounters from Hills & Fullerton (1980) investigate the energy and member exchanges between stars involved in three-body interactions. Other possible outcomes of three-body interactions are ionizations, where the binary

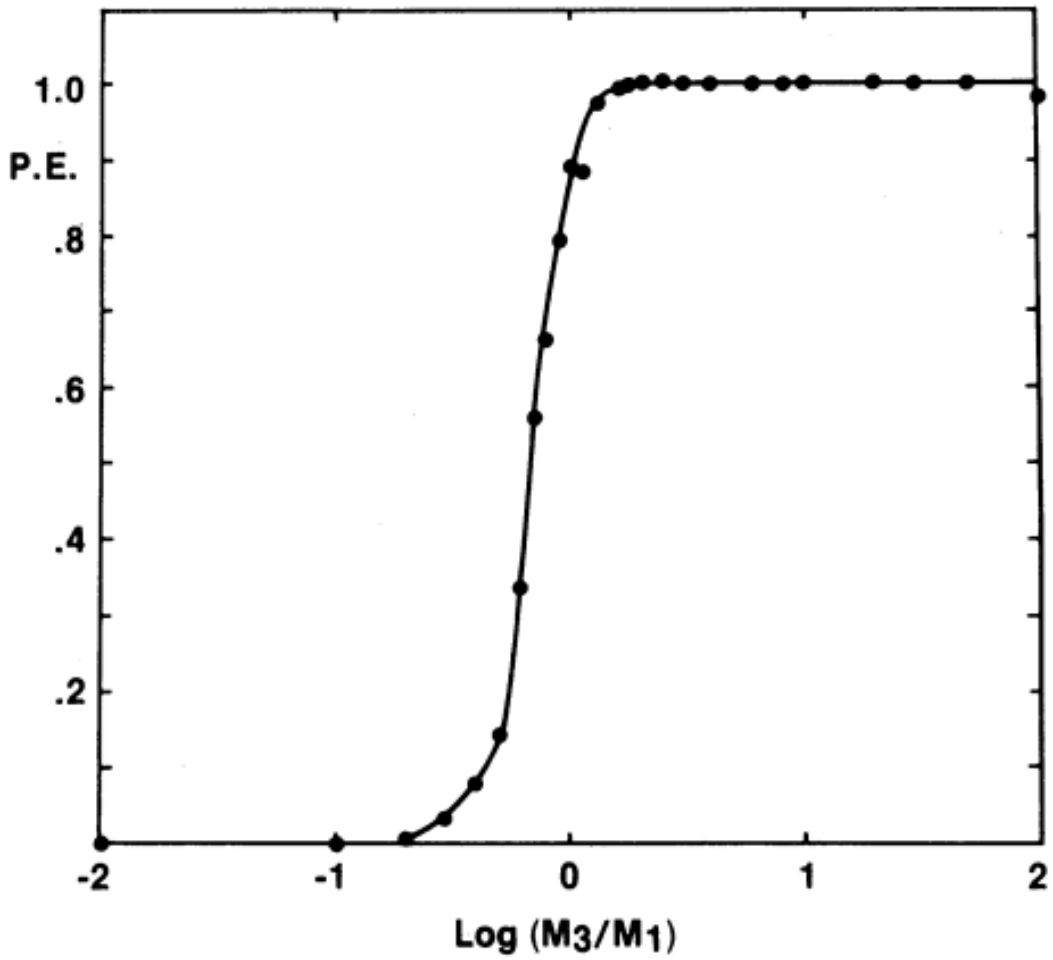

Figure 1.3: The exchange probability of a three-body encounter (expressed as a function of the mass of the intruder star as a fraction of the mass of one of the binary components). Figure reproduced from Figure 4 of Hills & Fullerton (1980).

is split up, and mergers, where components of the interactions merge. Ionizations are unlikely for hard binaries, requiring high energies to split the binary, and mergers mostly occur for small binary separations (e.g. Lützgendorf et al., 2012).

Exchanges and flybys can both result in the single star post-encounter gaining energy, resulting in a high-velocity star. This velocity will depend on the masses of the components involved, as the higher the mass, the more energy involved. An exchange will generally occur when the original single object has a higher mass than either of the components (as seen in Figure 1.3), indicating that if one of the binary components have a larger mass than the interloper, a flyby is more likely. Within the cores of globular clusters, the highest mass objects would be stellar-mass black holes which dynamically interact with nearby stars, forming binaries around the hard-soft limit (e.g. Antonini et al., 2019). In this case, dynamical three-body encounters involving black holes are more likely to include the black hole in a binary, indicating that flybys would be the dominant result of three-body interactions with a black hole.

1.3 High-Velocity Stars

Black holes and other stellar remnants in clusters are not typically detectable through the usual spectroscopic or photometric means. In order to constrain the remnant population of globular clusters and investigate the potential of black hole mergers in clusters, we can utilize high-velocity stars ejected from the cores of these clusters. The velocities of the high-velocity stars ejected are tracers for the bodies involved in their ejection, thus observations of high-velocity stars could be used to identify black holes populations.

1.3.1 Identifying High-Velocity Stars

Past work in the field, namely Lützgendorf et al. (2012) and Meylan et al. (1991), had the goal of identifying high-velocity stars originating in the clusters NGC 2808 and NGC 104, respectively. To identify a high-velocity star, one needs a velocity measurement, either from astrometry (proper motions) or spectroscopy. These works utilized radial velocity data, which is found using spectroscopic methods and the Doppler shift to measure the velocity of a star in the radial direction towards or away from the Earth perpendicular to the plane of the sky. Spectroscopic measurements can usually only be made for relatively bright stars in globular clusters. For example, in the case of Lützgendorf et al. (2012) the stars were all brighter than magnitude 17 in the V-band, as shown in Figure 1.4, which only includes brighter red giants and horizontal branch stars. A high-velocity star in each case is defined as having a velocity 3σ away from the cluster's mean velocity, with σ being the cluster's velocity dispersion. If a star is around 3σ or more from the typical star velocity in a cluster, it is very unlikely to originate from the cluster's Maxwellian velocity distribution. High-velocity stars are expected to be ejected isotropically from the cluster core, thus only a fraction of the high-velocity stars produced will have a high velocity along the line of sight. The other dimension of velocity is proper motion velocity in the plane of the sky, composed of two components, generally Right Ascension (RA) and Declination (Dec). Proper motion measurements compose 2 out the the 3 components of the 3d velocity vector, and thus may capture more high-velocity stars which are ejected isotropically than radial velocity measurements can. Radial velocity data is

considerably more difficult to obtain than proper motion data, and thus the number of stars in a cluster with radial velocity data available is generally not as large as the number of stars with proper motion measurements since the *Gaia* mission (Gaia Collaboration et al., 2016). The advantage to using radial velocity data is that stars with most of their velocity in the radial component will be either in front of or behind the cluster and close to the cluster centre in projection on the plane of the sky, making them easier to locate. Stars with a high velocity in proper motion will move far from the cluster on the sky, and thus will only be visible for a brief period of time post-ejection in a region of the sky surrounding a cluster. In general, proper motion velocity measurements have an advantage on radial velocity measurements for identifying high-velocity stars, as data can be found for more stars.

Stars identified as having a high velocity which are found in the vicinity of a globular cluster may not be genuine high-velocity stars produced by three-body interactions. Many of these stars identified may not be originating from the cluster at all, but may be foreground or background stars (i.e. contaminants). In order to determine potential cluster membership for high-velocity star candidates, past works such as Lützgendorf et al. (2012) and Meylan et al. (1991) placed their candidates on the Colour-Magnitude Diagram (CMD) for the cluster of potential origin. High-velocity stars would have properties consistent with that of the originating cluster, such as their placement on the CMD. All the candidate stars for Lützgendorf et al. (2012) appeared to belong to the cluster CMD, seen in Figure 1.4. Other checks for cluster membership which have been utilized in the past include checking that the stars have tangential velocities consistent to that of the cluster (Lützgendorf et al.,

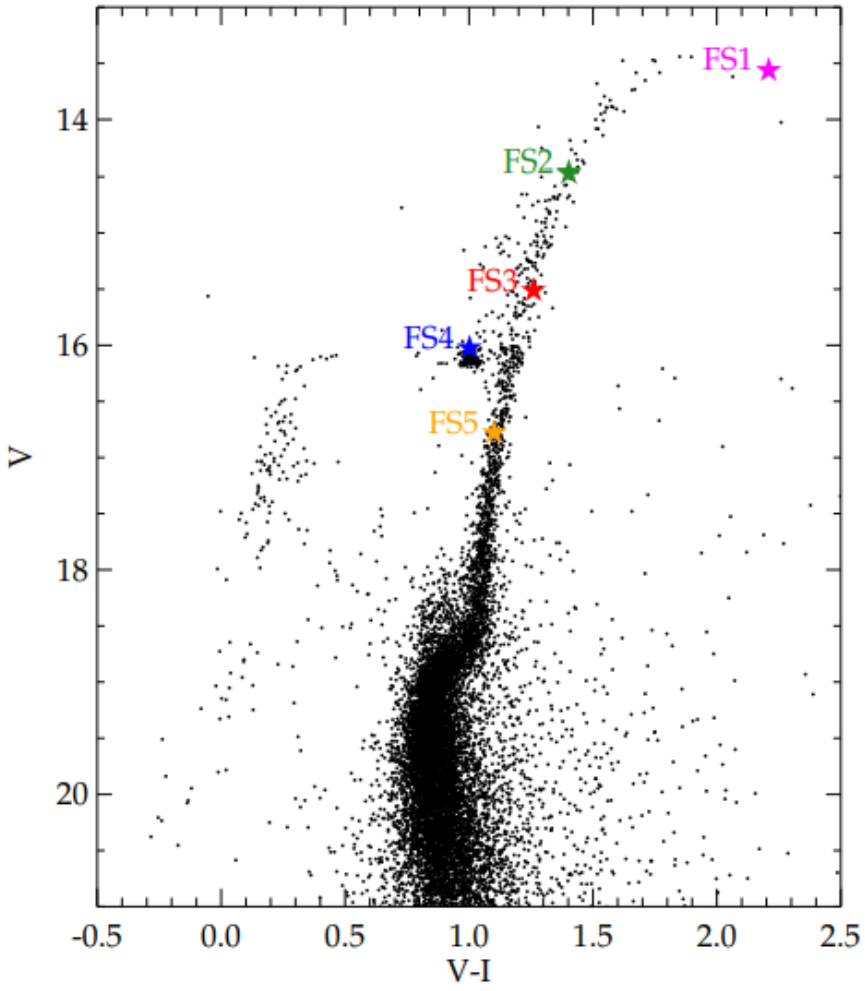

Figure 1.4: A Colour-Magnitude Diagram of NGC 2808, with the high-velocity star candidates overplotted. Figure reproduced from Figure 4 of Lützgendorf et al. (2012).

2012), and evaluating the density of contaminant stars in the region to determine the probability of a star being a contaminant (Meylan et al., 1991).

1.3.2 Origins of High-Velocity Stars

The specific numbers and velocities of observed high-velocity stars can be used to place constraints on the environment they were ejected from. The quantities which influence the number of high-velocity stars ejected from a cluster include the number

of black holes and other stellar remnants present in the cluster, the binary fraction, and the core density (e.g. Lützgendorf et al., 2012; Fragione & Gualandris, 2019). Only a fraction of high-velocity stars produced will actually be observable depending on the specifics of the method of observation. Factors which influence the detectability include the velocity components measured (for example only a fraction of stars ejected will have a high velocity in proper motion), the brightness/magnitude range of the observations, the area investigated for high-velocity stars, and the likelihood that a high-velocity star may get lost in the contaminant population of stars. The specific energy or velocity of a high-velocity star depends on the properties of the binary and single object which ejected it, including the masses of the components and the semi-major axis of the binary.

Past works have evaluated possible acceleration mechanisms for observed high-velocity stars. Lützgendorf et al. (2012) determined that two-body relaxation is unlikely, leaving dynamical three-body encounters as the primary acceleration channel for their observed high-velocity stars. They evaluated the possibility that these stars were accelerated via the exchange method, using numerical three-body scattering experiments, specifically the SIGMA3 STARLAB package (Hut et al., 2010). Scattering a binary composed of two 0.8 $M_{\odot}$ stars with an object of varying mass, Lützgendorf et al. (2012) determined that the most likely origin of the stars observed among the scenarios investigated was a binary star system interacting with a black hole, resulting in one of the binary stars being ejected at a high velocity.

1.4 This Thesis

The goal of this thesis is to investigate the possible black hole population of globular clusters by looking for the signature of high-velocity stars ejected by dynamical three-body interactions. In order to detect high-velocity stars, we will be using proper-motion velocity data from the Gaia satellite in the vicinity of all the Milky Way globular clusters. This data will be filtered based on properties of high-velocity stars and the cluster they originate from, as described in Chapter 2. In order to evaluate the possibility of the observed high-velocity stars being ejected from interactions involving black holes, we utilize the properties of binaries in order to predict the velocity distribution of stars ejected from a cluster core for different combinations of interacting objects, as outlined in Chapter 3. The results of the observational high-velocity stars selection and a comparison to the analytic velocity distributions is presented in Chapter 4. A discussion of the origins of the observed high-velocity stars, and a comparison with the high-velocity star rates and black hole population from past works is presented in Chapter 5. The results are summarized in Chapter 6 along with potential directions for future work.

Chapter 2

Methods: Extracting High-Velocity Star Candidates from Gaia Data

The process described in this chapter is partly based upon research conducted over the Summers of 2021 and 2022, with significant modifications.

2.1 Data Retrieval

In order to identify high-velocity stars around Milky Way globular clusters, we will not utilize radial velocity data like in previous works (Meylan et al., 1991; Lützgendorf et al., 2012), but will use proper motion data from the *Gaia* mission, which has the potential to capture more high-velocity stars than can be found using radial velocity measurements. The most recent data release of Gaia, Data Release 3 (DR3) includes stars up to magnitude limit of about G=20 (Gaia Collaboration et al., 2022a), making it well-suited for observing stars around Milky Way globular clusters (Gaia Collaboration et al., 2016, 2022a,b). In order to detect high-velocity stars, the region to study in the *Gaia* DR3 archive must be determined. This was selected to be a circle in Right Ascension (RA) and Declination (Dec) around each cluster centre (from the Baumgardt Structural Parameters Catalogue[1]) with a radius of twice the cluster's tidal radius listed in the Baumgardt Structural Parameters Catalogue,

[1] `https://people.smp.uq.edu.au/HolgerBaumgardt/globular/parameter.html`

based on equation 8 of Webb et al. (2013). This value allows for the maximum amount of cluster stars to remain in the sample while limiting the effect of contaminants. This sample is restricted to only include stars with good quality Gaia data. These filters restrict the following parameters to the specified ranges, based on the procedure from Vasiliev & Baumgardt (2021b): we limit the significance of excess noise of the source to be low (`astrometric_excess_noise_sig` < 2.0), constrain the renormalised unit weight error (`ruwe` < 1.15), ensure that the fraction of successful Image Parameters Determination windows with more than one peak is low to limit binary stars (`ipd_frac_multi_peak` < 2), ensure the number of visibility periods used is large enough to avoid excess errors (`visibility_periods_used` $>$ 10), constrain the G-band magnitude to not be excessively bright (`phot_g_mean_mag` > 13), and limit the goodness of fit amplitude to ensure the star is not a double star (`ipd_gof_harmonic_amplitude` $<$ exp[0.18(`phot_g_mean_mag` - 33)]). The Gaia documentation for the definition of these parameters is accessible on their website[2].

2.2 Filtering Based on Cluster Properties

From this general star sample in the vicinity of each cluster, filters are applied to remove non-members of the cluster and only include potential high-velocity star candidates. A star is defined as being a high-velocity star candidate if it has a total proper motion velocity (the magnitude of the 2d velocity vector in the plane of the sky relative to the cluster centre) greater then three times the cluster's central veloc-

[2] `https://gea.esac.esa.int/archive/documentation/GEDR3/Gaia_archive/chap_datamodel/sec_dm_main_tables/ssec_dm_gaia_source.html`

ity dispersion listed in the Baumgardt Structural Parameters Catalogue (Baumgardt, 2017; Sollima & Baumgardt, 2017; Baumgardt & Hilker, 2018; Sollima et al., 2019; Vasiliev & Baumgardt, 2021b). The sample was also filtered to only include stars with a possible parallax value (within uncertainties) corresponding to a distance from the cluster along the line of sight within twice the cluster's tidal radius.

High-velocity stars ejected from a globular cluster must originate from the dense cores of these clusters where the 3-body interactions and ejections take place. Every high-velocity star candidate should thus be able to be traced back to the cluster core using their proper motion velocities. In order to check for an origin in the cluster core, we defined the core as being a circular region with radius equal to the core radius defined in Spitzer (1987) as the radius at which the surface brightness is half its central value and adopted the values from the Baumgardt Structural Parameters Catalogue. In order to determine whether the core of the cluster is a possible origin of the star, a series of lines is created to trace back the possible past positions of the star from its proper motion measurements, within 1-σ uncertainties. If any of the past positions is within the cluster core, or if the values enclose the cluster core, the star is defined as being of potential core origin.

In order to ensure the high-velocity candidate originated from the cluster core, and is not heading towards the core, the angle of the star's trajectory is considered. The angle of the star's path is defined as the angle the star is moving from the 'horizontal', or $\theta_1 = \tan\left(\frac{\mathrm{PM_{Dec}}}{\mathrm{PM_{RA}}}\right)$, where $\mathrm{PM_{Dec}}$ and $\mathrm{PM_{RA}}$ refers to the proper motion in Declination and Right Ascension, respectively. The secondary angle is the angle

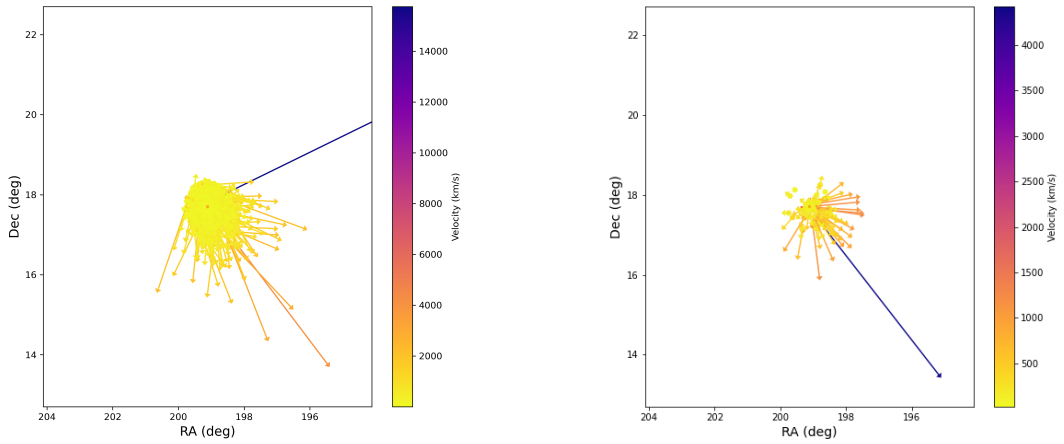

(a) Pre-Filter

(b) Post-Filter

Figure 2.1: The positions of the stars before and after the direction of motion and cluster core origin selection filters for the cluster NGC 5053. The arrows indicate the direction of motion of the stars in the plane of the sky. The plot is centered on the core of the cluster.

from the cluster core to the star's position, defined as $\theta_2 = \tan\left(\frac{\mathrm{Dec_{star}} - \mathrm{Dec_{cluster}}}{\mathrm{RA_{star}} - \mathrm{RA_{cluster}}}\right)$. The star is defined as originating from the cluster core if these two angles are within 20° of each other, an upper limit which will capture the direction of motion of the stars given that most stars in the sample are a significant distance from the cluster core at their present-day position. This criteria indicates that the star's direction of motion matches an origin in the cluster core when paired with the criterion described in the previous paragraph. The results of this selection on a sample cluster, NGC 5053, are shown in Figure 2.1, both before and after the filter is applied. All the high-velocity star candidates remaining after this filter can be traced back to a possible origin in the cluster core.

Stars which are members of a globular cluster generally lie in high-density regions of that cluster's colour-magnitude diagram, or CMD. A CMD of a population of stars

like those in a globular cluster traces out a specific path, an isochrone corresponding to the different brightnesses and colours for various initial stellar masses for stars all of the same age. Any high-velocity stars candidates should lie in a region of high density of cluster member stars in the originating cluster's CMD, and those which do not are most likely contaminants. The data to construct the CMD for each Milky Way globular cluster was taken from Vasiliev & Baumgardt (2021a) as the G magnitude brightness and BP-RP colour parameters. This data includes a list of stars in the region of each cluster with their membership probability to belong to that cluster. From this original list of clusters we only retain for further analysis the clusters with a CMD that is sufficiently populated, specifically if there are at least 1000 stars with over 50% membership probability. A CMD constructed with less stars than this does not have a well-defined locus, and cannot be used as a reference to assess the cluster membership/origin of high-velocity star candidates. In total, 96 globular clusters contain a sufficient number of likely member stars in the Gaia catalogue to construct a CMD. The `scipy.stats` function `kde.gaussian_kde` was utilized to estimate the density of the member stars as a function of BP-RP colour and G-band magnitude. The density corresponding to the colour and magnitude of each high-velocity candidate star was found, and if this was in a sufficiently high-density region of the CMD (a density of over 5% the maximum density of the CMD), the star was retained. An example of this process can be seen in Figure 2.2. The stars in regions of low density are shown with black points and are excluded from the final high-velocity star sample, while the stars shown in red are considered possible cluster members. Appendix A illustrates these two filters, the direction-of-motion filter and

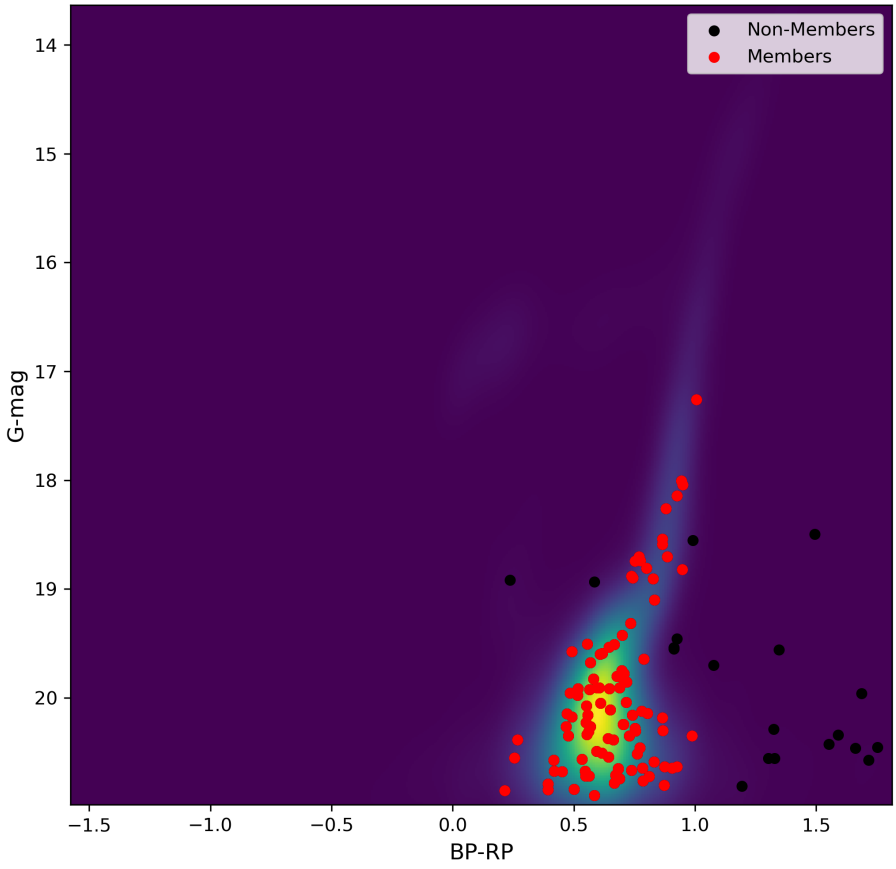

Figure 2.2: A kernel density estimate plot of the CMD for this star cluster, NGC 5053. The stars identified as non-members are shown as black points, while those in red are possible cluster members according to their position on the CMD.

the CMD membership filter for the clusters selected for further analysis in Chapter 4,

along with the filter discussed in Section 2.3.

2.3 Fitting the Distribution of Cluster and Contaminant Populations in Proper Motion Space

The stars within a globular cluster share certain properties, related to their age, masses, and positions on the sky, which have been utilized to select high-velocity star candidates and distinguish them from contaminant non-members as detailed in the previous section. The stars in a globular cluster also share a common motion within the galaxy (although stars in a cluster also move relative to each other such that their velocity will differ from the systemic velocity of the cluster as a whole). Plotting their velocities in proper motion coordinates of Right Ascension and Declination (as can be seen in Figure 2.3 for the cluster NGC 6121), the cluster can clearly be seen as an overdensity of stars with similar velocities in the centre of the figure corresponding to the cluster's systemic proper motion across the sky. In this example, a secondary population of stars is clearly visible in the upper right of the figure. This population of stars is more extended in proper-motion space, and is interpreted as a contaminant population, with no relation to the cluster but observed in the vicinity of the cluster in projection on the sky despite being at a different distance. Some of these contaminant stars may by chance fall on the cluster's CMD and not have been removed by the selection process described in the Section 2.2. In order to remove any high-velocity star candidates that belong to the contaminant population from the sample, the distribution of these two populations in proper-motion space must be characterized

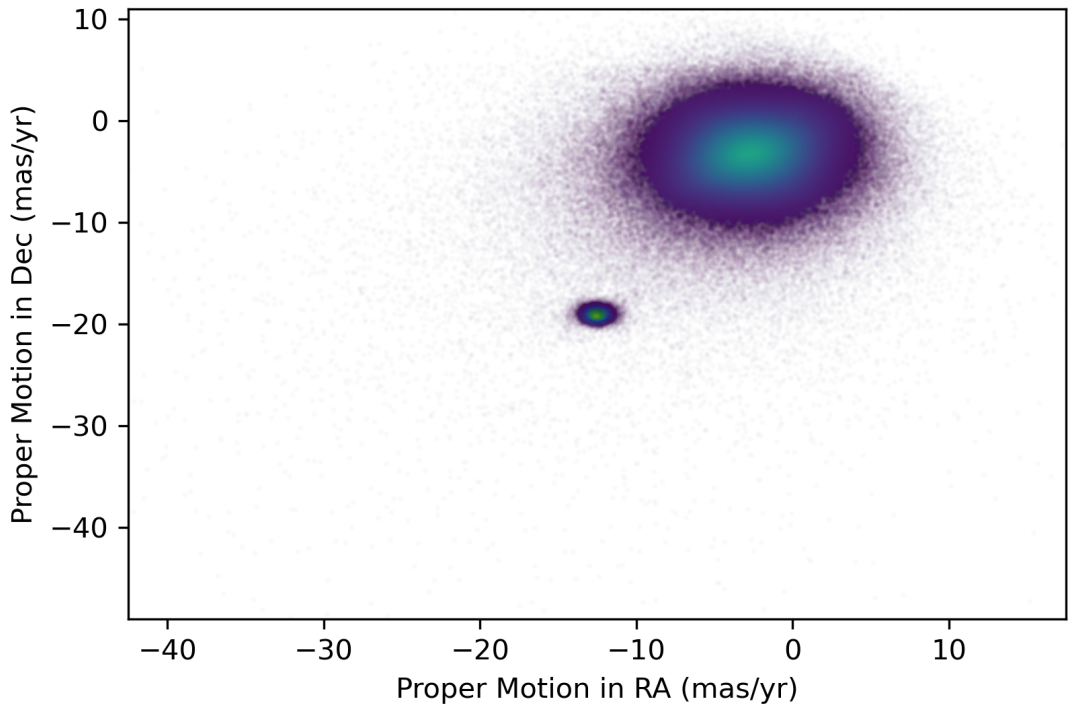

Figure 2.3: A plot of the distribution of stars in the region of a globular cluster, NGC 6121, in proper motion space. The central population is composed of cluster members stars, while the other population of composed of other stars in the galactic plane.

by fitting a multi-component model to the proper motion distribution of stars within the region of interest of each cluster. In order to do this, the Nested Sampling code `Dynesty`[3] is used (Speagle, 2020). The data utilized to fit the populations was the sample of stars from Section 2.1, with the CMD filter from Section 2.2 applied. This dataset was used as it represents the stars in the cluster region which have the same intrinsic distribution as the high-velocity candidates in the sample. The distribution of stars in proper motions is assumed to be composed of two populations. The first population is assumed to be a two-dimensional Gaussian representing the cluster, which has the same standard deviation along both axes and no covariance or

[3] `https://doi.org/10.5281/zenodo.7215695`

correlation between the two dimensions. The probability of finding a cluster member with proper motions in Right Ascension and Declination μ_α and μ_δ is:

$$p_{\text{cluster}}(\mu_\alpha, \mu_\delta) = \frac{e^{-\frac{1}{2}(x-\mu)^T \Sigma^{-1}(x-\mu)}}{\sqrt{(2\pi)^k |\Sigma|}}, \tag{2.1}$$

where k is the number of dimensions (2); μ, the mean of the distribution is the vector $\begin{bmatrix} \overline{\mu}_\alpha \\ \overline{\mu}_\delta \end{bmatrix}$, x is the vector $\begin{bmatrix} \mu_\alpha \\ \mu_\delta \end{bmatrix}$, and Σ, the covariance matrix in 2 dimensions is $\begin{bmatrix} \sigma^2_{cluster} + \mu^2_{\alpha error} & 0 \\ 0 & \sigma^2_{cluster} + \mu^2_{\delta error} \end{bmatrix}$, $\overline{\mu}$ represents the mean of the Gaussian in proper motion RA (α) or Dec (δ) dimensions, μ and μ_{error} represent the proper motion and proper motion errors of the star (in RA (α) and Dec (δ)) and $\sigma_{cluster}$ is the spread of the Gaussian. Three variables thus need to be fitted in order to define the Gaussian, the means of the proper motions in Right Ascension and Declination μ_α and μ_δ, along with the standard deviation of the Gaussian distribution $\sigma_{cluster}$ describing the intrinsic width of the proper-motion distribution of the cluster.

For the second population, the probability of finding a star with proper motions in Right Ascension and Declination α and δ is defined as:

$$p_{\text{contaminants}}(\mu_\alpha, \mu_\delta) = [\frac{\Gamma(-\frac{1}{2} - \frac{\tau}{2})}{\Gamma(-1 - \frac{\tau}{2})}]^2 \frac{\{[1 + \frac{\mu_x}{a_x}^2][1 + \frac{\mu_y}{a_y}^2]\}^{\frac{(1+\tau)}{2}}}{\pi a_x a_y}, \tag{2.2}$$

where μ_x and μ_y are:

$$\mu_x = (\mu_\alpha - \overline{\mu}_\alpha)\cos\theta + (\mu_\delta - \overline{\mu}_\delta)\sin\theta, \tag{2.3}$$

and

$$\mu_y = -(\mu_\alpha - \overline{\mu}_\alpha)\sin\theta + (\mu_\delta + \overline{\mu}_\delta)\cos\theta. \tag{2.4}$$

This probability distribution is based on equations 23 and 24 of Vitral (2021) defining a Pearson VII distribution. Vitral (2021) and references therein reason that this distribution is a good choice to represent the contaminant population, since it has wider wings than a Gaussian which allows it to better capture the spread of a contaminant population. μ_α and μ_δ are respectively the proper motions in Right Ascension and Declination of the dataset, $\overline{\mu}_\alpha$ and $\overline{\mu}_\delta$ are the mean proper motions of the population being modelled, a_x and a_y are the semi-major and semi-minor axes of the distribution, θ is the tilt of the Pearson VII distribution from the x-axis, and τ is a constant, the slope of the distribution.

These two distributions, the Gaussian cluster distribution combined with the contaminant Pearson VII distribution, result in 10 free parameters to constrain: three for the Gaussian ($\overline{\mu}_{\alpha,cluster}$ and $\overline{\mu}_{\delta,cluster}$, the Gaussian means in RA and Dec and $\sigma_{cluster}$, the Gaussian spread), six for the Pearson VII distribution ($\overline{\mu}_{\alpha,contaminants}$ and $\overline{\mu}_{\delta,contaminants}$, the Pearson VII means in RA and Dec, a_x and a_y, the semi-major and semi-minor axes, θ, the tilt of the Pearson VII distribution from the x-axis, and τ, the slope of the distribution), plus one additional free parameter for the amplitude, the strength of the contaminant compared to the cluster such that the probability of finding a star with proper motions μ_α and μ_δ is

$$p(\mu_\alpha, \mu_\delta) = (1 - A)p_{\text{cluster}}(\mu_\alpha, \mu_\delta) + Ap_{\text{contaminants}}(\mu_\alpha, \mu_\delta). \tag{2.5}$$

The priors set on the free parameters are assumed to be uniform priors with the following bounds:

i) $\overline{\mu}_{\alpha,cluster}$ is assumed to be within the 1-σ uncertainty range of the Right Ascension proper motion of the cluster from the Baumgardt Structural Parameters Catalogue.

ii) $\overline{\mu}_{\delta,cluster}$ is assumed to be within the 1-σ uncertainty range of the Declination proper motion of the cluster from the Baumgardt Structural Parameters Catalogue.

iii) $\sigma_{cluster}$ is assumed to range from $\frac{1}{10}$x to 3x the cluster's central 1d velocity dispersion from the Baumgardt Structural Parameters Catalogue.

iv) $\overline{\mu}_{\alpha,contaminants}$ has a prior which simply constrains it to be within the range of the proper motion Right Ascension values of the data being fitted.

v) $\overline{\mu}_{\delta,contaminants}$ has a prior which simply constrains it to be within the range of the proper motion Declination values of the data being fitted.

vi) a_x is constrained to be minimum zero, maximum the width of the data on its widest axis, Declination or Right Ascension.

vii) a_y is constrained to be minimum zero, maximum the width of the data on its widest axis, Declination or Right Ascension.

viii) θ is constrained to be between 0 and π.

ix) τ by definition is less than -2, thus it is constrained to be between -2 and $-\infty$.

x) A, The relative amplitude of the two populations is always between 0 and 1.

The nested sampler `Dynesty` estimates the posterior, or the probability of the model parameters given the data (and priors) (Speagle, 2020). We use the nested sampler version of `Dynesty` (Skilling, 2004; Skilling, 2006), multiple ellipsoidal bounds

(Feroz et al., 2009), and random slice sampling (Neal, 2003; Handley et al., 2015a,b). The sampler provides the user with the estimated posterior distribution, and the mean value of the posterior samples for each parameter can be evaluated to find the best-fitting parameters.

Using these `Dynesty` fits, we revisit the high-velocity star candidates found through the previous sections. The probability of a star with given proper motion measurements of belonging to the cluster population relative to the contaminant population can be computed using Equation 2.1 and Equation 2.2, incorporating the relative amplitudes of the likelihoods. The Gaussian membership probability formula, Equation 2.1, incorporates the errors on the data as two Gaussians (the intrinsic distribution and the Gaussian to describe the error on the data) which are simple to convolve, however the Pearson VII formula (Equation 2.2) cannot include this convolution analytically, and thus does not account for the uncertainty on the data. The uncertainty on the proper motion velocities can be significant, effectively broadening the probability distribution of observing a contaminant star with proper motions in RA and Dec μ_α and μ_δ. If not taken into account, this could alter the relative probability of belonging to the cluster population or the contaminant population. In order to account for the uncertainties when computing the probability of finding a star from the contaminant population with proper motions in RA and Dec μ_α and μ_δ, the Pearson VII distribution is convolved numerically with a Gaussian error distribution. The formula for convolving a 2-dimensional function is:

$$(f * g)(x, y) = \int_{-\infty}^{\infty} \int_{-\infty}^{\infty} f(\alpha, \beta) g(x - \alpha, y - \beta) d\alpha d\beta \tag{2.6}$$

where x and y are the proper motion (Right Ascension and Declination) values to evaluate the error-corrected likelihood for, i.e. the high-velocity star candidates, while α and β are the variables of integration encompassing the total proper motion space. f is the Pearson VII probability density function, Equation 2.2, with μ_{alpha} and μ_{delta} as the variables of integration, α and β. $g(x-\alpha, y-\beta)$ is the Gaussian error function of the star's proper motion measurement, defined as Equation 2.1, and adapted to be

$$PDF = \frac{e^{-\frac{1}{2}(x)^T \Sigma^{-1}(x)}}{\sqrt{(2\pi)^k |\Sigma|}}. \tag{2.7}$$

k is the number of dimensions (2), x is the vector $\begin{bmatrix} x - \alpha \\ y - \beta \end{bmatrix}$ (variables defined above), the covariance matrix in 2 dimensions is $\begin{bmatrix} \alpha_{error}^2 & 0 \\ 0 & \delta_{error}^2 \end{bmatrix}$, with α_{error} and δ_{error} being the 1-σ uncertainties of the proper motion measurement of the candidate in the Right Ascension and Declination components respectively.

Once the likelihood of a star belonging to either the cluster or the error-corrected contaminant population is found, we evaluate the relative likelihood of each star belonging to either population. The likelihoods are normalized by their amplitudes, and converted into a percentage probability by dividing by the total likelihood, as

depicted in Equation 2.8.

$$p_{\text{cluster}}\% = \frac{(1-A)\, p_{\text{cluster}}(\mu_\alpha, \mu_\delta)}{(1-A)\, p_{\text{cluster}}(\mu_\alpha, \mu_\delta) + A p_{\text{contaminants}}(\mu_\alpha, \mu_\delta)} \text{x} 100\% \tag{2.8}$$

Any star with a cluster membership probability above 50% is considered a high-velocity star candidate. These fits and the high-velocity star candidates for the clusters selected for analysis in Chapter 4 are displayed in Appendix A.

Chapter 3

Predicting the Velocity Distribution of High-Velocity Stars

The high-velocity star candidates identified in the previous chapter could be produced by a number of different three-body interactions. In order to evaluate what velocities may be produced by different masses of single and binary bodies, we utilize analytic properties of binaries and interactions. We determine the velocity distribution of stars ejected from a binary system without using scattering experiments, by making assumptions about the nature of the binaries in the cluster and their binding energy. The change of binding energy of a star system with time, $\frac{dE_b}{dt}$, is uniform as the hardening rate of binaries is constant with time (e.g. Antonini et al., 2019), which corresponds to an constant increase of binding energy with time until the binary reaches the minimum possible semi-major axis. This allows us to assume that the number of binaries at each binding energy, $\frac{dN}{dE_b}$ is constant. The binding energy of a binary can be connected to the velocity gained by a single star during a three-body interaction.

The binaries we investigate, which are mostly stellar remnant binaries, are assumed to dynamically formed at the hard-soft limit. This sets an upper limit to the binary semi-major axis and thus a lower limit to the binding energy of the binary $E_{\rm b,min} = E_{\rm b,hardsoft}$. The upper limit to their binding energy is set by the minimum

semi-major axis a binary system can attain, a_{min}, which is the semi-major axis at which the binary will merge (for low-mass, large-radius, stellar binaries involving stars), or be ejected from the cluster (for higher-mass stellar remnant binaries). During a binary-star interaction, a fraction of this binding energy will be transformed into momentum of the binary center-of-mass and single star. The energy change in a binary-star interaction is on average 0.2 E_b (e.g. Antonini et al., 2019). The binary and the single star get a 'kick', which can be determined through momentum conservation. This kick is related to the amount of binding energy in the binary, which is greater for binaries with more massive components. The upper limit to the binding energy and thus energy exchange is also larger for a binary with more compact components, as their minimum semi-major axis is set by their semi-major axis of ejection rather than the larger radius-dependant merger semi-major axis which limits the minimum semi-major axis for stellar binaries.

In order to get a velocity distribution for the ejected stars from three-body interactions with a specific type of binary, the cluster's probability density function for the velocity of the ejected stars is found. The velocity distribution follows from conservation of number

$$f(v) = \frac{dN}{dv} = \frac{\partial N}{\partial E_b(v)} \left| \frac{\partial E_b(v)}{\partial v} \right|, \tag{3.1}$$

where $f(v)$ is the velocity distribution of stars ejected by the three-body interaction investigated, N is the number of stars, v is the ejection velocity of the single star in the interaction, and E_b is the binding energy of the binary, Equation 1.1. The

hardening rate of binaries, $\frac{dE_b}{dt}$ is approximately constant with time (e.g. Antonini et al., 2019), thus $\frac{dN}{dE_b(v)}$ should be some constant, k. In order to determine $\left|\frac{dE_b(v)}{dv}\right|$, a formula is found that relates v, the velocity of the star ejected, to the binding energy of the binary. The velocity of the star we are concerned about is the kick velocity the star (m_3) receives from a binary. The average kick a binary gets from a scattering three-body interaction assuming the average energy exchanged in an interaction is 0.2 E_b is $v_{2-1}^2 = 0.2G\frac{m_1m_2}{m_1+m_2+m_3}\frac{m_3}{m_1+m_2}\frac{1}{a}$, based on equation 13 from Antonini et al. (2019), while the velocity the interloper single star attains is $v_{int} = \frac{m_1+m_2}{m_3}v_{2-1}$ (Miller & Lauburg, 2009). From these equations, the typical velocity the single star gains in the interaction can be written as

$$v_{int} = \frac{m_1+m_2}{m_3}\sqrt{0.2G\frac{m_1m_2}{m_1+m_2+m_3}\frac{m_3}{m_1+m_2}\frac{1}{a}} = \sqrt{0.2G\frac{m_1m_2}{m_1+m_2+m_3}\frac{m_1+m_2}{m_3}\frac{1}{a}}, \tag{3.2}$$

by replacing v_{2-1} in the above formula. In order to get this formula in terms of E_b, some of the common variables (m_1, m_2 and a) and constants (G) in the v_{int} formula can be substituted in favour of E_b, Equation 1.1, to obtain

$$v_{int} = \sqrt{0.4\frac{m_1+m_2}{m_1+m_2+m_3}\frac{E_b}{m_3}}. \tag{3.3}$$

Thus, E_b in terms of v_{int} is $E_b = \frac{5}{2}v_{int}^2 m_3\frac{m_1+m_2+m_3}{m_1+m_2}$, and $\frac{dE_b}{dv}$ is $\frac{dE_b}{dv} = 5v_{int}m_3\frac{m_1+m_2+m_3}{m_1+m_2}$, and $f(v)$ will be

$$f(v) = kv_{int}m_3\frac{m_1+m_2+m_3}{m_1+m_2} \tag{3.4}$$

for some normalization constant k. To normalize the probability density function,

Equation 3.4 is integrated over the possible range of velocities. v_{min} comes from the maximum possible semi-major axis value, at the hard-soft limit, $\frac{1}{2}\langle m\rangle\sigma^2 \approx E_b = \frac{Gm_1m_2}{2a}$ (Heggie & Hut, 2003), thus the hard-soft limit semi-major axis is $a_{\mathrm{hard-soft}} = \frac{Gm_1m_2}{\langle m\rangle\sigma^2}$. $\langle m\rangle$ is the average mass of stars in the cluster, and σ is the velocity dispersion, which in the cluster core would be close to the central velocity dispersion. Similarly, v_{max} comes from the minimum possible semi-major axis value, which depends on the mass of the binary components. For two stars in a circular orbit, the semi-major axis is half the distance between them, which has a rough minimum in a circular orbit equal to the average of their radii, approximated as $R = 0.8(\frac{m}{M_\odot})^{0.7}R_\odot$ (Habets & Heintze, 1981). For a system with a red giant star, anything around 1 $M_\odot$ in an $\sim$12 Gyr-old globular cluster, the minimum semi-major axis is taken to be around 100 $R_\odot$, an estimate for a red giant radius. If the objects in the binary are both compact, then the minimum semi-major axis is the semi-major axis the binary will be ejected due to recoil, with a_{ej}

$$a_{ej} \approx 0.1AU(\frac{m_1m_2}{m_1+m_2+m_3}\frac{m_3}{m_1+m_2}\frac{0.6}{M_\odot})(\frac{50km/s}{v_{esc}})^2, \tag{3.5}$$

and where v_{esc} is the escape velocity of the cluster where the interaction takes place. It will be ejected from the cluster at this separation as when the binary interacts, the single object and the binary both gain momentum in opposite directions and the binary recoil velocity can exceed the cluster's escape velocity at this semi-major axis (Antonini & Rasio, 2016; Antonini et al., 2019). Using these semi-major axes limits as boundaries for the velocity, the normalization constant can be found for each

interacting system. The normalized $f(v)$ in the case where a 0.8 $M_\odot$ star interacts with a binary composed of a 0.8 $M_\odot$ star and an object of a range of different input masses is shown in Figure 3.1. The maximum velocity of this function can be seen to

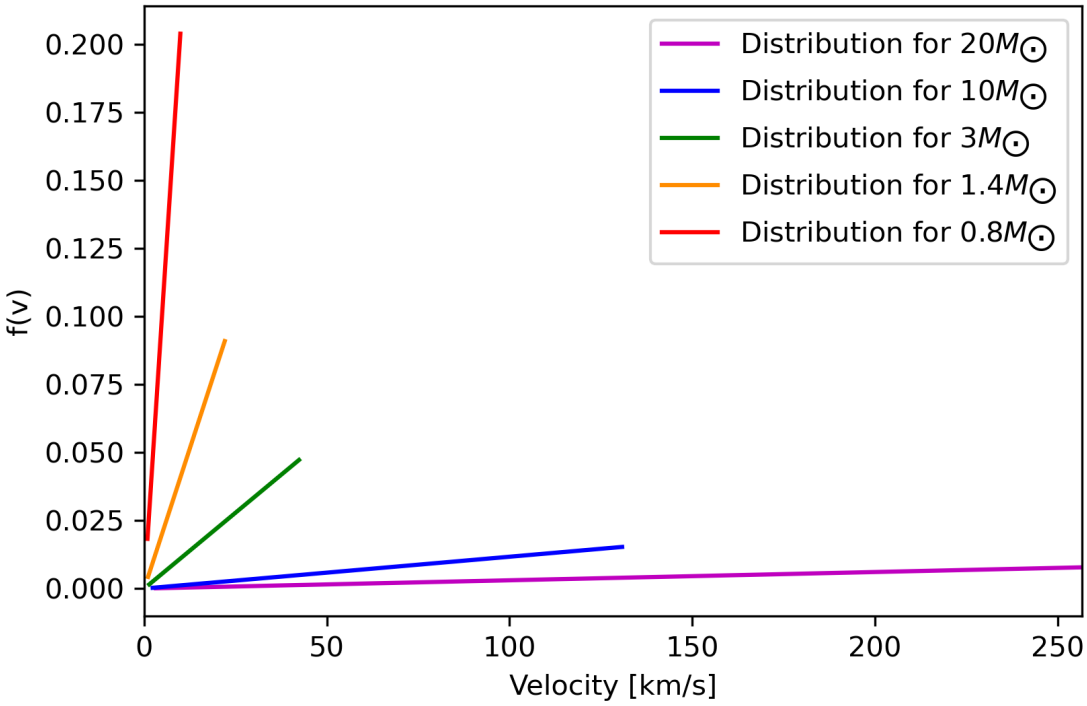

Figure 3.1: A plot of the ejection velocity probability density function of different interactions studied for the values of the cluster NGC 6838. The interactions studied are that of a 0.8 $M_\odot$ star interacting with a binary composed of a 0.8 $M_\odot$ star and an object which varies in mass for each line, with a mass of 20 $M_\odot$, 10 $M_\odot$, 3 $M_\odot$, 1.4 $M_\odot$, or 0.8 $M_\odot$.

decrease with decreasing mass of the binary components.

This velocity probability density function ($f(v)$) provides the velocities which the star is ejected at and their relative probabilities, but as the star moves out of the cluster's gravitational potential it will slow down. To quantify this effect, we approximate the mass density distribution of the cluster as a Plummer sphere, $\rho(r) = \frac{3M_0}{4\pi a^3}(1 + \frac{r^2}{a^2})^{-\frac{5}{2}}$ (Plummer, 1911). M_0 is the total cluster mass, and a is defined as

being $\frac{r_c}{0.64}$, where r_c is the core radius of the cluster (Dejonghe, 1987). In order to find the slowing force the cluster exerts on an outwards-moving star, the gravitational force formula is applied, $dF = \frac{GmdM}{r^2}$, with dM being ρdV, with dV for a sphere as $dV = 4\pi r^2 dr$, and ρ as the Plummer density profile. Integrating dM to get M from the centre of the cluster to an arbitrary radius, r, the mass enclosed is $M(< r) = M_0 r^3 (a^2 + r^2)^{-\frac{3}{2}}$. The force will thus be:

$$F = -GmM_0 r(a^2 + r^2)^{-\frac{3}{2}}, \tag{3.6}$$

where the negative sign implies that it is directed inwards. This is the force from the mass enclosed within a sphere with the radius being the star's current distance from the core. In order to compute the velocity as a function of the distance from the the centre of the cluster, $v(r)$ must be found in terms of the known $F(r)$, $\frac{F(r)}{m} = \frac{dv(r)}{dt} = \frac{dv(r)}{dr}\frac{dr}{dt} = \frac{dv(r)}{dr}v(r)$. From this, the kinematic formula for integration is $\int_{r_0}^{r} \frac{F(r)}{m} dr = \frac{v^2 - v_0^2}{2}$, where r_0 and v_0 are the initial radius and velocity at the time of ejection. Integrating $\frac{F(r)}{m} = GM_0 r(a^2 + r^2)^{-\frac{3}{2}}$ gives $v(r)$:

$$v(r) = \sqrt{v_0^2 - 2GM_0(\frac{1}{a} - \frac{1}{\sqrt{a^2 + r^2}})}. \tag{3.7}$$

In order to turn the ejection velocity probability density function into an observable velocity distribution for high-velocity stars seen in proper motion in a given cluster and take into account geometric effects, we generate random stars from this probability distribution and retain only stars which would have be identified in our

data. We take an initial set of binary parameters, m_1, m_2, m_3, and $\langle m \rangle$. The values needed for each cluster are r_c, the core radius to define the a parameter of the Plummer model, r_t, the tidal radius to determine the size of the field view being investigated for high-velocity stars (2 r_t), M_{clust}, the cluster's mass to use in $v(r)$ calculations for M_0 in Equation 3.7, v_{esc}, the cluster's escape velocity to use in the a_{min} calculations in Equation 3.5, and σ_{clust}, the central velocity dispersion to use in the definition of a high-velocity star, $v > 3\sigma_{clust}$. All these values for the selected cluster are taken from the Baumgardt Catalogue. A star is randomly drawn from the ejection velocity probability density function, Equation 3.4, within the velocity bounds. This star is ejected from the cluster core at this initial velocity, with a random 3d orientation described by θ_{star}, between 0 and π, and ϕ_{star}, between 0 and 2π. A random time is selected for how long ago the star was ejected, T_{ej} anywhere between 0-15 Myr ago, as any stars ejected earlier than this are no longer in the region of investigation. An approximation is made that $v(r) = \frac{\delta r}{\delta t}$, thus $\delta r = \delta t v(r)$ in order to determine how the velocity changes with radius and time within a small time interval δt. This equation is applied to solve $v(r)$ of Equation 3.7 for a step size of $\frac{1}{1000}^{th}$ the time since the star was ejected, T_{ej} until the time gets to be around the present time. This velocity is the 3d velocity in space of the simulated star at this time. In order to get the position of this star in terms of the sky coordinates used observationally, RA and Dec, the spherical coordinates equations are applied, x = r $\sin(\theta_{star})$ cos (ϕ_{star}), y = r $\sin(\theta_{star})$ sin (ϕ_{star}), and z = r $\cos(\theta_{star})$, where x, y, and z are the positions or velocities in RA, Dec, and along the line of sight respectively. The radius in RA-Dec space is ensured to be within the visible range for the region, $2r_t$,

and the velocity in proper motion RA-Dec space is checked to ensure is it defined as a high-velocity star, where $v > 3\sigma_{clust}$. Figure 3.2 shows the 2d velocity distribution of all stars ejected from an interaction (a 0.8 $M_\odot$ star interacting with a 0.8 $M_\odot$ and 20 $M_\odot$ binary) in black, and the stars which remain in the $2r_t$ region in blue. This figure illustrates how the stars with larger velocities are less likely to be in the region of investigation at the current time, compared to the slower-moving stars which spend a greater amount of time in the region. For each cluster, we assume $\langle m \rangle$ is 0.6 $M_\odot$. The

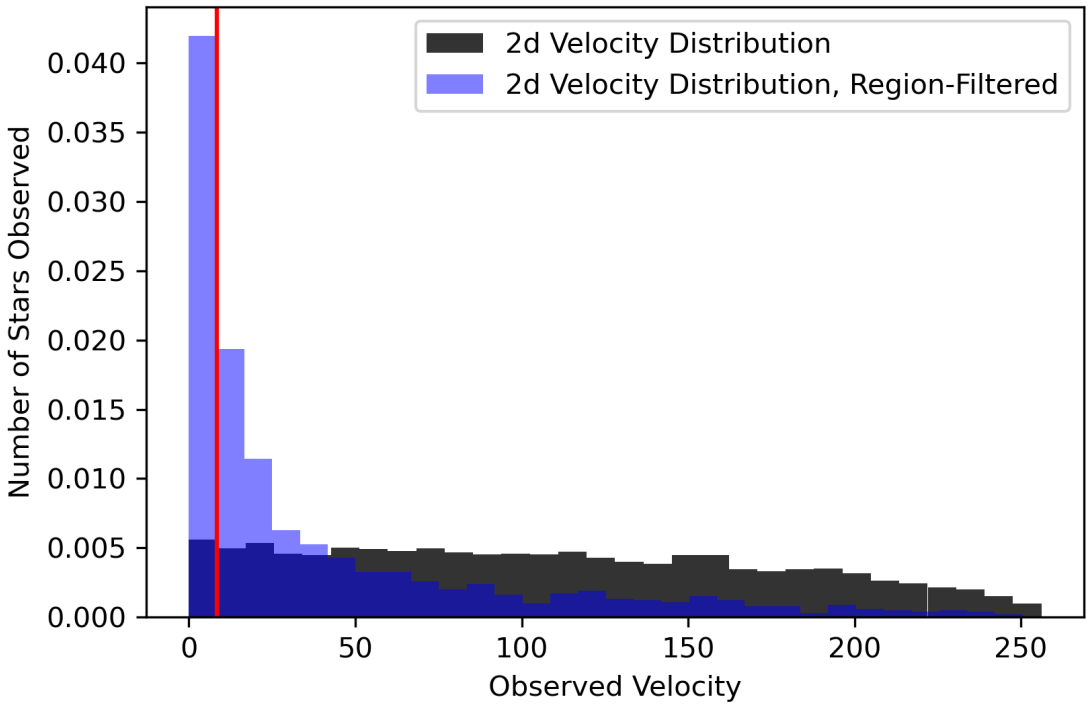

Figure 3.2: This figure displays the probability density function for a sample of stars ejected from a 0.8 $M_\odot$ star interacting with a 0.8 $M_\odot$ and 20 $M_\odot$ binary, for a sample cluster. The black bars show the 2d distribution in the plane of the sky of all stars ejected from this interaction, while the blue bars show the 2d distribution in the plane of the sky of the stars ejected from this interaction which remain in the $2r_t$ radius. The red line indicates the high-velocity limit for the cluster.

encounters examined are that of a 0.8 $M_\odot$ star interacting with a binary where one

of the components is another 0.8 $M_\odot$ star, and the other component's mass varies. This mass is chosen to represent a star in the cluster which has not yet evolved into a stellar remnant, at around the main sequence turnoff for most globular clusters. The masses evaluated are a 20 $M_\odot$ black hole, a 10 $M_\odot$ black hole, a 3 $M_\odot$ black hole, a 1.4 $M_\odot$ neutron star, and a 0.8 $M_\odot$ star. Figure 3.3 illustrates the different

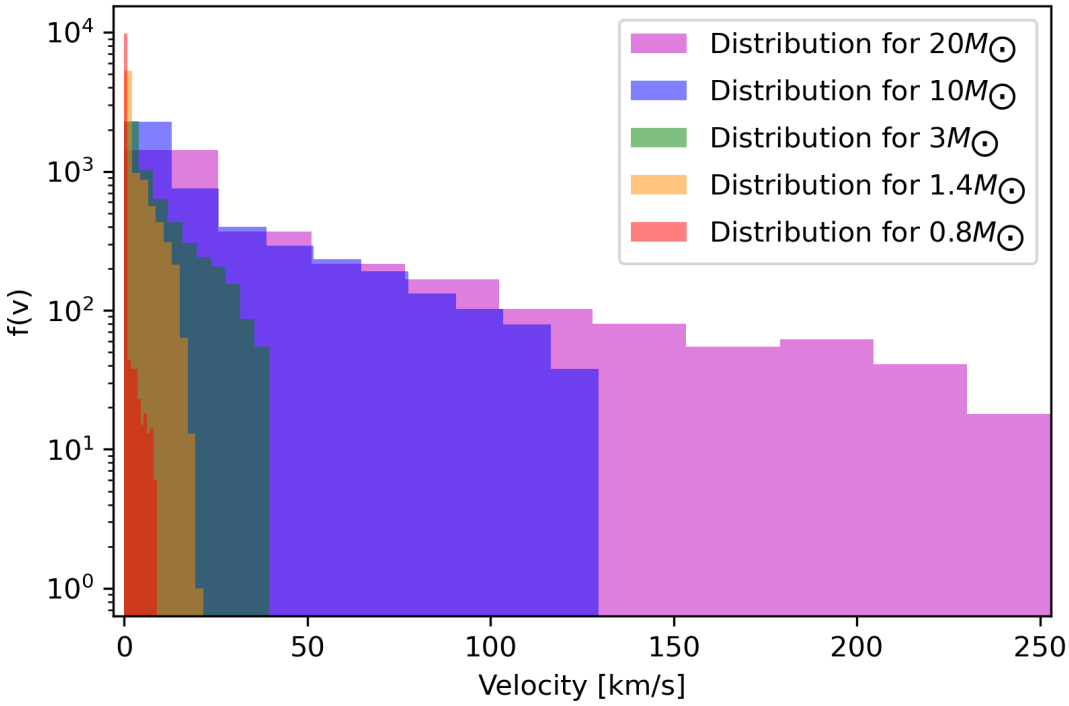

Figure 3.3: This figure displays the probability density function for a sample of stars in the cluster NGC 6838 ejected from a variety of different interactions. The interactions included are that of 0.8 $M_\odot$ star interacting with a 0.8 $M_\odot$ and an object which varies in mass for each colour, with a mass of 20 $M_\odot$, 10 $M_\odot$, 3 $M_\odot$, 1.4 $M_\odot$, or 0.8 $M_\odot$. The velocities are the 2d distribution in the plane of the sky of the stars ejected from these interactions which remain in the $2r_t$ radius.

2d velocity distributions of stars in the $2r_t$ radius for the cluster NGC 6838, for all the interactions investigated.

Chapter 4

Results: Comparing Observations and Theoretical Predictions

4.1 Quality of the Fits to the Proper Motion Distributions

Section 2.3 described how we characterize the distribution of the cluster members and contaminants in proper motion space, for each cluster being investigated. The degree to which these populations are separable and distinct from one another varies. The fits of the variables discussed in Section 2.3 can vary, in some instances the best fitting value for a variable, particularly the cluster dispersion, σ_{clust} can be at the bound restricted by the prior. In that case the σ_{clust}, which should not be larger than the prior bounds allow for, cannot be fully trusted. This likely indicates that the contaminants and cluster members overlap significantly in proper motion space, and the fitted 'cluster' population does actually contain a significant contribution from contaminants. In these cases, the degree to which the fits can be relied upon to provide a clear picture of which stars might be high-velocity stars and which ones are likely contaminants is low. A cluster like that displayed in Figure 4.1 has clearly distinct populations, while one like in Figure 4.2 is an extreme case where the cluster is completely lost in the contaminant population.

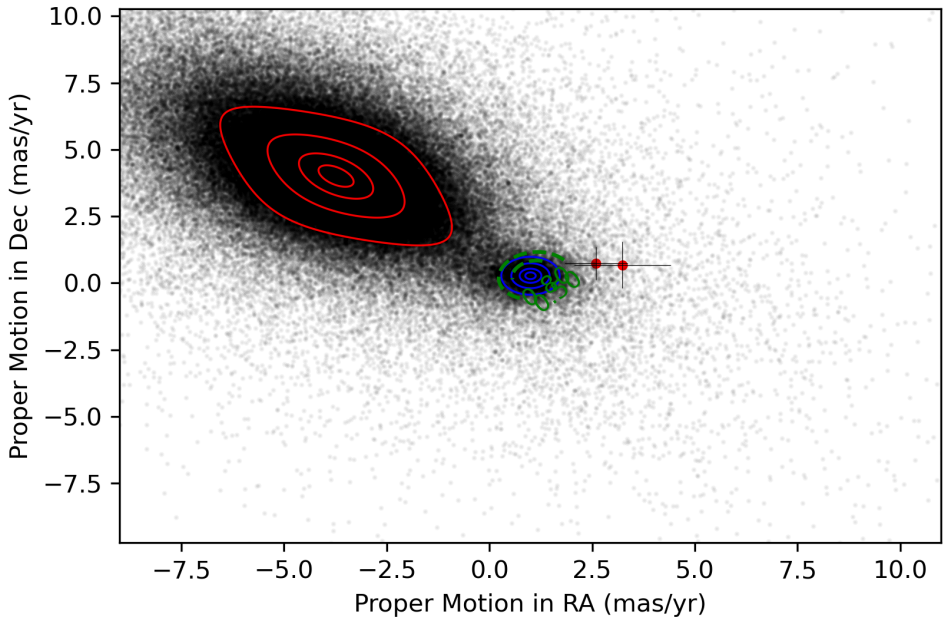

Figure 4.1: The cluster NGC 2808 is the central overdensity of stars in proper-motion space, with the fit to its proper-motion distribution represented by the blue contours. The red contours represent the fitted contaminant population for this cluster, while the green dashed contours are a representation of where a star might be equally likely to be a cluster star or contaminant star, 80% likely to belong the cluster, and 95% likely to belong to the cluster, calculated using the probability procedure from Section 2.3. The two high-velocity candidates found for this cluster are in red, with the errors on the proper motion measurements represented by the faint grey lines.

Most clusters lie somewhere between these two extreme cases, with a cluster partially hidden by a contaminant population. In the interest of using well-constrained results for the analysis, we visually selected 13 out of the 53 globular clusters with high-velocity candidate stars which have well-constrained fits and distinct populations. There were a number of additional motivations to remove a particular cluster from this 'gold sample', namely issues with the data collected, more than two populations of stars present in the proper motion data, or a cluster population which is poorly fit by a symmetric 2d Gaussian. The 13 clusters in our 'gold sample' for

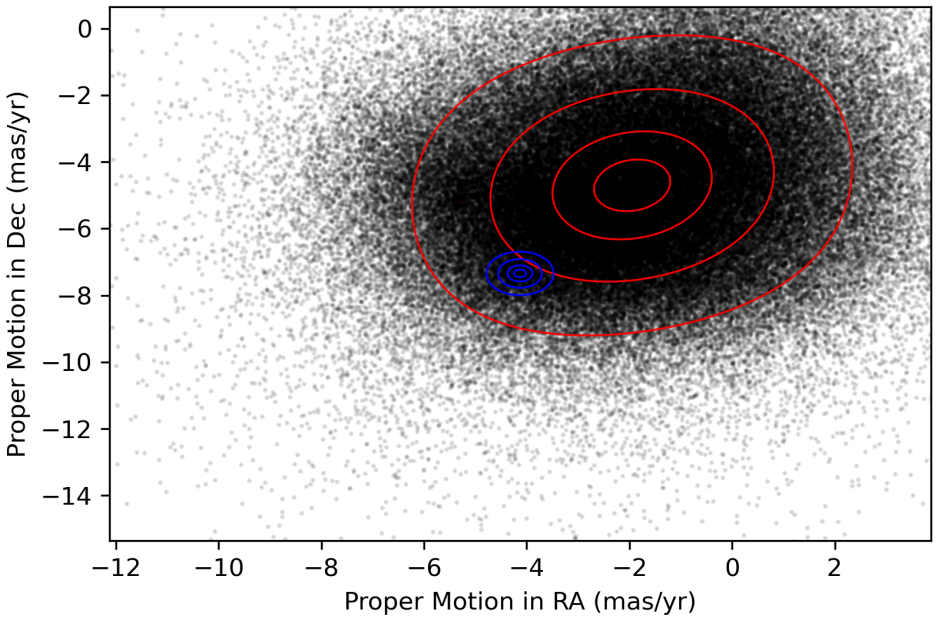

Figure 4.2: The cluster NGC 6569 is the central overdensity of stars in proper-motion space, with the fit to its proper-motion distribution represented by the blue contours. The red contours represent the fitted contaminant population for this cluster, calculated using the probability procedure from Section 2.3. This cluster is very difficult to distinguish from the background contaminant population.

more in-depth analysis are FSR 1758, NGC 2298, NGC 2808, NGC 3201, NGC 4372, NGC 4590, NGC 5286, NGC 6541, NGC 6626, NGC 6652, NGC 6779, NGC 6809, and NGC 6838.

4.2 Observed High-Velocity Star Candidates

96 clusters had the `dynesty` population match filter applied in order to determine whether stars were more likely to be cluster members or contaminants (Section 2.3). Out of these 96 clusters, 43 of them had no high-velocity star candidates remaining after only retaining stars likely to be cluster members based on their proper motion

using this selection. The other 53 clusters each have between 1 and 344 candidates, with a total of 2137 amongst all 53 clusters. Each high-velocity star candidate for a cluster has a probability of being a cluster member star based on its proper motion, and is retained as a high-velocity star candidate if its probability of being a member of the cluster is greater than 0.5, or 50%. However, one has to keep in mind that these stars still have a non-zero probability of being a contaminant, their false positive probability which is $1 - p_{\text{cluster}}$.

Table 4.1 contains a summary of all clusters with high-velocity star candidates. It lists the number of candidates found for each cluster, the fraction of high-velocity stars in the cluster which may be false positives based on their individual membership probabilities, and a summary of the quality of their fits, namely the reason a cluster was removed from the 'gold sample'.

Table 4.1: A summary of the details of every cluster found to have high-velocity star candidates

Cluster	Number of Candidates	False Positive Fraction	Gold	Notes
BH 140	42	0.16	No	Cluster σ peaks at top bound of prior
FSR 1758	3	0.47	Yes	-
IC 4499	34	0.24	No	Cluster σ peaks at top bound of prior
NGC 104	86	0.26	No	More than 2 populations in region
NGC 288	139	0.07	No	Cluster σ peaks at top bound of prior
NGC 362	46	0.10	No	More than 2 populations in region
NGC 1261	42	0.19	No	Populations not well separated
NGC 1851	30	0.37	No	Populations not well separated
NGC 1904	34	0.21	No	Populations not well separated
NGC 2298	31	0.14	Yes	-
NGC 2419	54	0.24	No	Cluster σ peaks at top bound of prior
NGC 2808	2	0.47	Yes	-

NGC 3201	84	0.04	Yes	-
NGC 4147	18	0.18	No	Populations not well separated
NGC 4372	2	0.22	Yes	-
NGC 4590	80	0.09	Yes	-
NGC 4833	7	0.09	No	Populations not well separated
NGC 5024	183	0.08	No	Cluster population has non-Gaussian distribution
NGC 5053	67	0.08	No	Cluster σ peaks at top bound of prior
NGC 5139	17	0.28	No	More than 2 populations in region
NGC 5272	153	0.12	No	Populations not well separated
NGC 5286	1	0.44	Yes	-
NGC 5634	21	0.21	No	Cluster σ peaks at top bound of prior
NGC 5824	3	0.44	No	Populations not well separated
NGC 5897	3	0.15	No	Populations not well separated
NGC 5927	22	0.07	No	Cluster σ peaks at top bound of prior
NGC 6093	22	0.09	No	Populations not well separated
NGC 6101	1	0.11	No	Cluster σ peaks at top bound of prior
NGC 6144	120	0.41	No	Populations not well separated
NGC 6171	30	0.39	No	Populations not well separated
NGC 6205	38	0.42	No	Populations not well separated
NGC 6229	8	0.25	No	Cluster σ peaks at top bound of prior
NGC 6254	9	0.44	No	Populations not well separated
NGC 6333	1	0.02	No	Populations not well separated
NGC 6341	34	0.33	No	Populations not well separated
NGC 6366	1	0.48	No	Populations not well separated
NGC 6441	116	0.07	No	Cluster σ peaks at top bound of prior
NGC 6541	12	0.15	Yes	-
NGC 6569	1	0.00	No	Populations not well separated
NGC 6626	2	0.02	Yes	-
NGC 6652	1	0.44	Yes	-
NGC 6656	5	0.17	No	Issues with initial data retrieval
NGC 6715	344	0.38	No	Populations not well separated
NGC 6723	14	0.37	No	Populations not well separated

NGC 6749	47	0.17	No	Cluster σ peaks at top bound of prior
NGC 6752	4	0.46	No	Populations not well separated
NGC 6779	23	0.33	Yes	-
NGC 6809	54	0.36	Yes	-
NGC 6838	4	0.06	Yes	-
NGC 7078	2	0.48	No	Populations not well separated
NGC 7089	34	0.30	No	Populations not well separated
Ter 3	4	0.40	No	Populations not well separated
Ter 5	1	0.04	No	Populations not well separated

4.2.1 Comparing Observed Candidates to Analytical Distributions

In order to determine what origin our high-velocity star candidates may have, the velocity distribution which may be produced from different encounters of single stars and binaries was investigated for each cluster in the 'gold sample'. For each cluster, these velocity distributions are constructed for the high-velocity stars produced by a given interaction, and compared to the cluster's observed sample of high-velocity star candidates. The interactions investigated include three different cases with black home masses of masses 20 $M_{\odot}$, 10 $M_{\odot}$, and 3 $M_{\odot}$, one involving another compact object, a neutron star of mass 1.4 $M_{\odot}$, and one involves a star of mass 0.8 $M_{\odot}$. The results for a few selected clusters are displayed in Figures 4.3 to 4.6, and the full 'gold' sample is in Appendix B.

Stars are produced by interactions with these binaries, however for some clusters the maximum velocity produced by this combination of objects is less than the limit which defines a high-velocity star, $3\sigma_{clust}$ (displayed as a vertical line in the bottom panel for each cluster). If an interaction is capable of producing a star fast enough to be considered a high-velocity star, a distribution is shown. If an interaction can produce a high-velocity star, but has a very low rate to do so such that a distribution is difficult to construct from the method described in Chapter 3, a vertical line indicates the maximum possible velocity that the interaction can produce. For every cluster examined we show a velocity distribution for interactions involving a binary component with a mass of 20 $M_{\odot}$ and 10 $M_{\odot}$, however velocity distributions

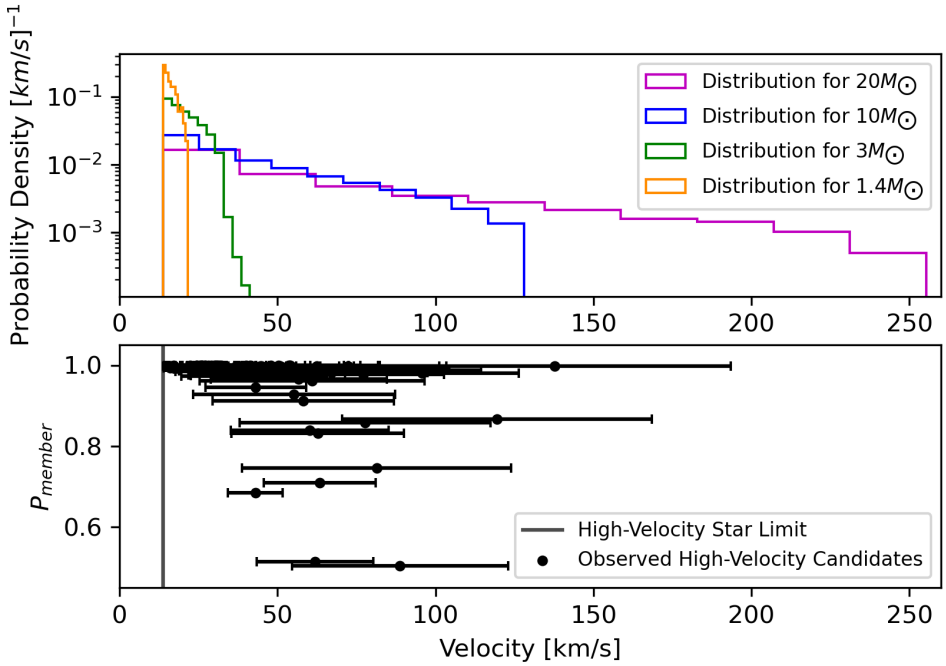

Figure 4.3: The velocity of the observed high-velocity star candidates, compared to the analytic velocity distribution for a range of binary masses, for the cluster NGC 3201. The distributions in the upper panel begin at the lower velocity threshold for a high-velocity star. These distributions are indicated by the coloured lines if sufficient stars are produced at a high velocity, or by a vertical line (indicating the theoretical maximum ejection velocity for a given interaction) if very few high-velocity stars are produced for a given interaction. The high-velocity star candidates for the cluster are displayed in the bottom panel, with their cluster membership probability on the y-axis.

for interactions involving lower-mass binary components are not always shown for the reasons described above for a given cluster. Only one of the 13 clusters in the gold sample can produce a high-velocity star velocity distribution from all the interactions examined, NGC 6838 in Figure 4.6. Eight clusters require interactions with a compact object of at least 1.4 $M_\odot$ to explain their high-velocity stars, which are the three black hole cases with 20 $M_\odot$, 10 $M_\odot$, and 3 $M_\odot$, along with the neutron star case of 1.4 $M_\odot$. These clusters are FSR 1758, NGC 2298, NGC 3201 (Figure 4.3), NGC 4372, NGC 4590, NGC 6652, NGC 6779 (Figure 4.5), and NGC 6809. Four clus-

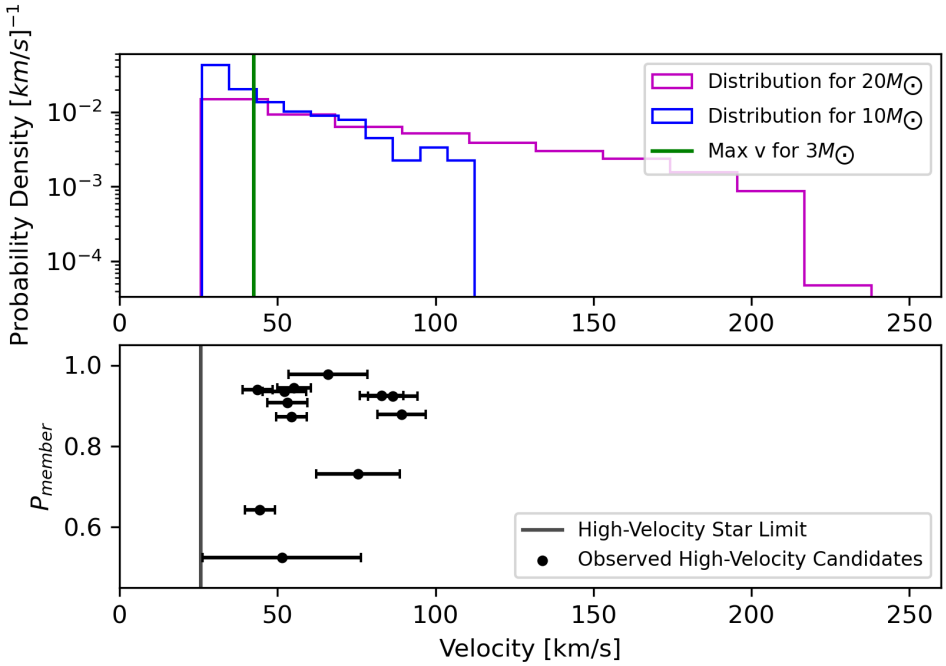

Figure 4.4: Same plot as Figure 4.3, for NGC 6541.

ters require interactions involving black holes to explain their observed high-velocity stars: NGC 2808, NGC 5286, NGC 6541 (Figure 4.4), and NGC 6626. The results for all clusters can be seen in Appendix B.

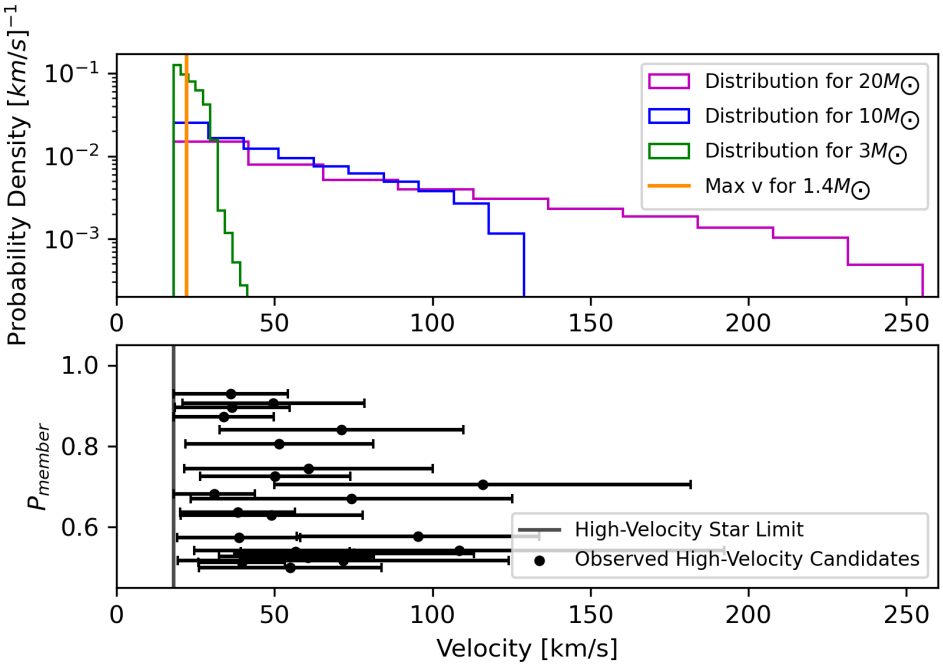

Figure 4.5: Same plot as Figure 4.3, for NGC 6779.

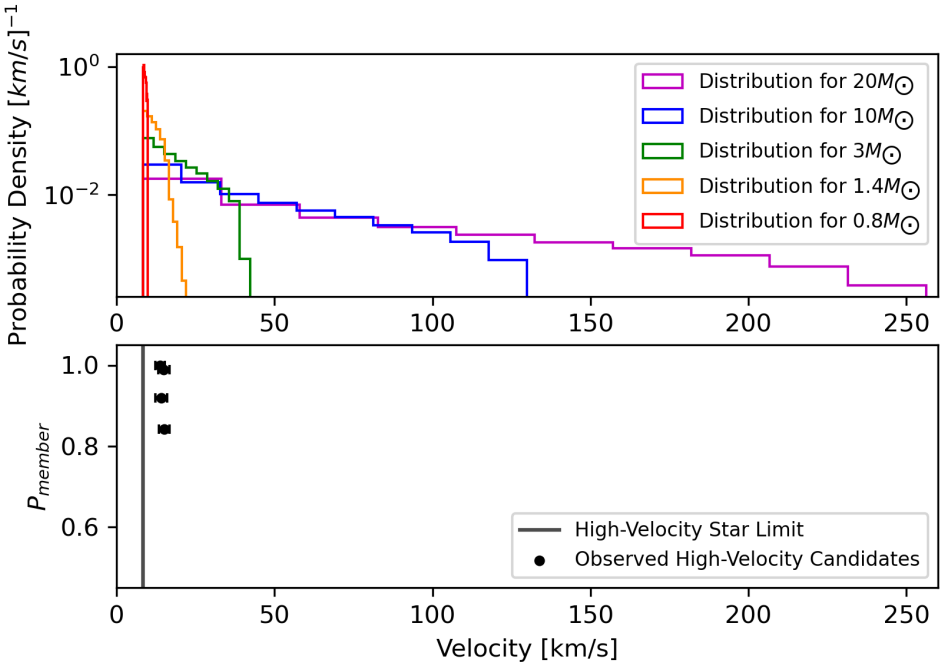

Figure 4.6: Same plot as Figure 4.3, for NGC 6838.

Chapter 5

Discussion

5.1 Likely Origins of Observed High-Velocity Stars

We assume that the observed high-velocity stars or a fraction of them may originate from interactions of the type described in Chapter 3, where a star interacts with a binary containing one star and one other object, in order to make conclusions about the origins of the stars. The observed high-velocity stars often have significant uncertainties on their proper motions as clearly illustrated in Figures 4.3 and 4.5. This makes it difficult to isolate which specific interaction may have ejected the stars, however for many clusters we may be able to identify the binary configuration which led to the ejection. Appendix B displays the predicted velocity distributions for all the clusters alongside their high-velocity stars, for reference.

For clusters such as FSR 1758, NGC 4372, NGC 6652, and NGC 6838, there are numerous possible origins for their high-velocity stars, including interactions with a binary containing a 1.4 $M_{\odot}$ neutron star. Figure 4.6 displays how the distributions overlap significantly at the relatively low velocity end for these particular high-velocity star candidates, making the star's origin uncertain. For many of these clusters, the only firm conclusion which can be made is that the high-velocity stars observed appear

to originate from interactions involving compact objects in globular clusters.

Other clusters, such as NGC 2298, NGC 3201, NGC 4590, NGC 6779, and NGC 6809 have some high-velocity stars which could come from all the possible interactions considered given uncertainties on their proper motions, but other stars can only be explained by interactions involving a black hole. The rest of the clusters from the gold sample, NGC 2808, NGC 5286, NGC 6541, and NGC 6626 all have black-hole interactions as the only possible ejection method for the high-velocity star candidates. From this we can conclude that these 9 clusters show observational evidence for hosting a black hole population. This research cannot make any conclusions about the number of black holes present in a given cluster without investigating the ejection rate of stars from three-body interactions, however some information about the masses of the black holes can be inferred. For a cluster such as NGC 6541, in Figure 4.4, some of the high-velocity star candidates are not consistent with originating from the low-mass 3 $M_{\odot}$ black hole ejection velocity distribution, only the distributions corresponding to interactions with higher-mass objects. NGC 2808 and NGC 6626 similarly have high-velocity stars only consistent with the higher-mass black hole interactions. The black hole population of these clusters must contain more massive black holes than 3 $M_{\odot}$.

5.2 Rates of High-Velocity Stars

Our analysis in the previous section demonstrated how we can use the velocity distribution of the observed high-velocity stars to make conclusion about the presence of

black holes in some clusters. To constrain the amount of the black holes in globular clusters, one would also need to consider the rates at which these interactions occur and their implications on the number of observed high-velocity stars as a function of velocity. A rough estimate of the realistic numbers of high-velocity stars expected in the region investigated can be compared to the numbers of observed high-velocity stars we have found to verify that these numbers are reasonable. Cabrera & Rodriguez (2023) investigates three-body scattering involving compact objects over the lifetime of globular clusters using Monte Carlo evolutionary dynamical models, with the goal of studying the extremely fast hypervelocity stars produced by these interactions. Their work investigates the rates at which interactions involving compact objects in three-body interactions occur across the lifetime of model clusters. They investigate 4 different cases of three body interactions involving compact objects which are either a black hole, neutron star or white dwarf. Two of the cases have one compact object, either as the single object or as one of the binary components (such as in our analysis), while the other two cases involve two compact objects, one of which is in the binary and the other as either the other binary component or as the single object. The authors conclude that the ejection rate of stars from compact object three-body interactions is around 0.00004 stars per year at the present day. This rate is that of all stars ejected from three-body interactions, while the observed high-velocity candidates from our sample may be limited to brighter stars as low-mass main sequence stars may not be bright enough to be detected. Thus, this rate is an upper limit of stars which are ejected which does not incorporate the detectability of the stars by the Gaia observatory. Over a time-frame of around 15 Myrs, which is the time-frame

over which all the stars studied in our work must have been ejected in order to remain in the region around the cluster analyzed, this rate corresponds to around 600 stars. These stars are the stars ejected from all types of three-body interactions, and these stars would not all be high-velocity stars. Which type of interaction is most likely to occur depends on the specific cluster, but we will assume that around $\frac{1}{4}$ of these stars come from a single star interacting with a binary where one of the components is a compact object, limiting the stars to around 150. Based on the velocity distributions we constructed in Chapter 3, between 0 to 20% of stars ejected by three-body interactions involving compact objects will have a high velocity and remain in the region of analysis. Overall, 0-15 high-velocity stars would be expected from a rough estimation based on this work and that of Cabrera & Rodriguez (2023), with an unknown fraction of these able to be detected by the Gaia telescope based on their brightness. For the clusters in the gold sample, there are between 1-84 observed high-velocity stars in proper motion velocity, which would be a fraction of those expected. The numbers of observed high-velocity stars that we have identified in several clusters are relatively consistent with the rough predicted values, within an order of magnitude.

5.3 Black Hole Populations of Globular Clusters

We have found evidence for the presence of black holes in nine globular clusters based on the velocities of high-velocity stars identified in the vicinity of these clusters. Past

works which have investigated the black hole populations of numerous clusters can be compared with our findings. Weatherford et al. (2020) is one such work which uses the fact that a large number of black holes is expected to suppress mass segregation among the visible stars to probe the black hole content of some Milky Way globular clusters. Figure 5.1 summarizes the results of Weatherford et al. (2020), along with those of

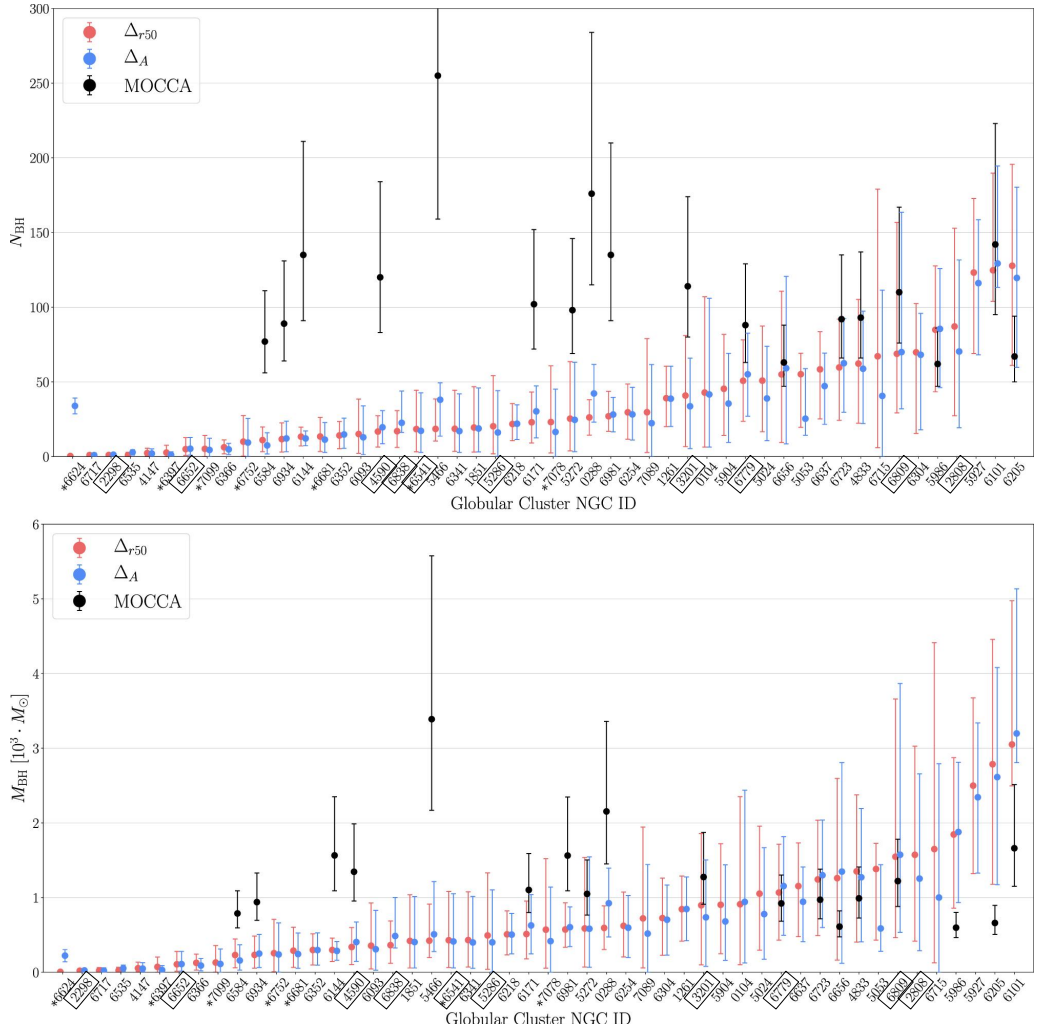

Figure 5.1: The predicted mass and number of black holes of the 50 globular clusters studied in Weatherford et al. (2020) in blue and red, from lowest to highest predicted numbers. The figure also includes similar results from the MOCCA survey in black (Askar et al., 2018). The ten clusters which overlap with our sample are indicated in black. Figure adapted from Weatherford et al. (2020).

another paper predicting black hole numbers from the structure of clusters, Askar et al. (2018) in black. Ten of the thirteen clusters in the gold sample are included in these figures, indicated in black. One of the clusters, NGC 2298 is consistent with having no black holes in these predictions, contradictory to the high-velocity stars we observe for this cluster which are only consistent with the presence of population of black holes. Many of the clusters in our gold sample which correspond to clusters in the Weatherford et al. (2020) selection have a moderate number of expected black holes. NGC 2808. NGC 3201, NGC 6779, and NGC 6838 have more expected black holes than most in the Weatherford et al. (2020) selection. The first three of these clusters are clusters which have high-velocity stars which can only be explained by interactions involving black holes. The last, NGC 6838 does not have any evidence from our high-velocity sample of the presence of black holes.

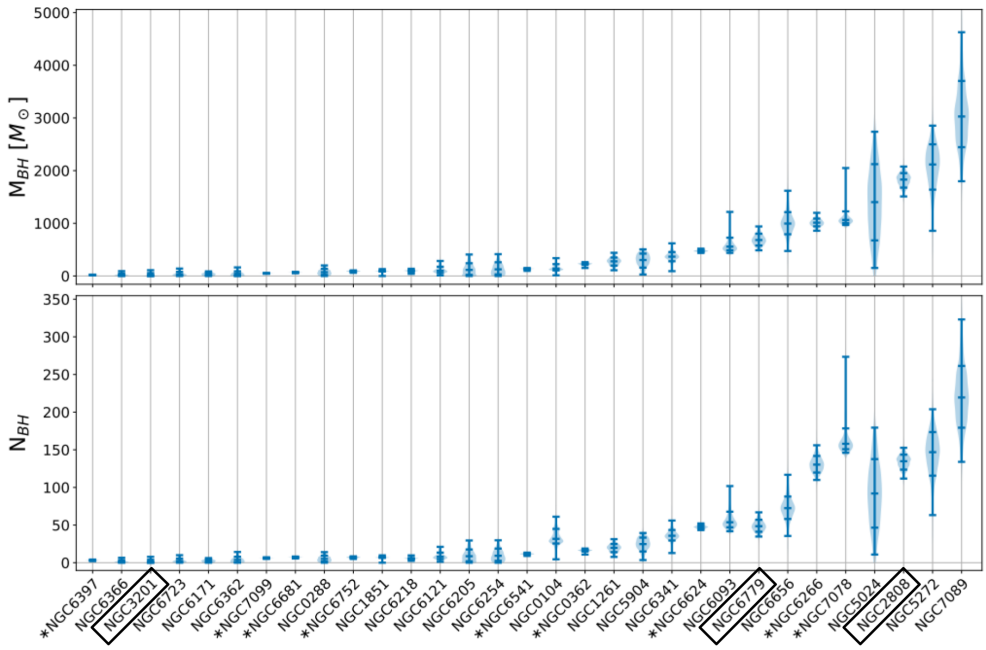

Figure 5.2: The predicted mass and number of black holes of the 31 globular clusters studied in Dickson (2022). The three clusters which overlap with our sample are outlined in black. Figure adapted from Dickson (2022).

Dickson (2022) has also utilized the distribution of stars to predict the number of black holes for a selection of Milky Way globular clusters. Figure 5.2 summarizes these results. Three of the clusters in the gold sample are includes in these figures, indicated in black. Based on our high-velocity stars, we expect all of these clusters to contain a population of black holes. One of these three clusters, NGC 3201 was found to have little-to-no black holes from the Dickson (2022) predictions, however the high-velocity stars we observe for this cluster are only consistent with the presence of population of black holes.

Chapter 6

Conclusion

The black hole and stellar remnant population of globular clusters can be difficult to determine, as these objects cannot generally be found through spectroscopic or photometric methods. In order to identify the presence of a population of black holes we can instead attempt to identify the fast-moving stars which have been ejected from the cluster through three-body interactions with black holes. Finding high-velocity stars and comparing them to the velocity distribution expected for different three-body interactions can allow for the identification of a potential black hole population within individual globular clusters.

In this thesis, we utilize *Gaia* Data Release 3 in order to locate high-velocity stars around Milky Way globular clusters. We retrieve all stars with good data within a region around each cluster which satisfy the criteria for being a high-velocity star, having a velocity greater then three times the cluster's central velocity dispersion. These stars are filtered to ensure they have the properties of cluster-originating high-velocity stars, including their direction of motion and placement on the cluster's Colour-Magnitude Diagram. The cluster and contaminant populations in proper-motion space are fitted and the high-velocity star candidates assigned a membership probability to the cluster in order to define a final sample. We find over 2000 high-velocity star candidates around the 53 clusters which contained candidates. Our gold

sample of thirteen clusters with good quality fits to the proper-motion distributions and with less suffering from contamination have between 1 and 84 high-velocity star candidates each.

The velocity distribution of ejected stars from three-body interactions where the single star and one of the binary components are 0.8 $M_{\odot}$, and the other binary component has varying mass, are modelled. The analytic velocity distribution for high-velocity stars detectable in the region of investigation around each cluster is created for each binary mass investigated and for every cluster in our gold sample. In all cases except one, there are no high-velocity stars produced above the velocity threshold unless there is a neutron star or black hole present in the binary.

Comparing these to the observed high-velocity stars, we find that many of the high-velocity stars could only be produced by interactions involving black holes, assuming these stars originate from the types of interactions studied. We thus find that for 9 clusters, NGC 2298, NGC 2808, NGC 3201, NGC 4590, NGC 5286, NGC 6541, NGC 6626, NGC 6779 and NGC 6809, a black hole population must exist. Our results for NGC 2808, NGC 6541, and NGC 6626 indicate that these clusters contain black holes greater than 3 $M_{\odot}$.

6.1 Future Work

There are a number of potential improvements on this work which could help expand the results. The selection procedure described in Section 2.3, in which we fit the proper motion populations in the region assumes the high-velocity stars will belong

to the Gaussian cluster population. Considering how large the velocities of these stars can be, that assumption is overly restrictive. In order to have a better model of the proper motions of the stars, the analytic velocity distributions from Section 3 could be applied to model the high-velocity stars alongside the cluster and contaminant populations. This step could also be improved for some clusters by incorporating more than one contaminant population. These improvements would retain more high-velocity stars in the sample which would yield more information on the black hole population within the clusters. It would also improve the number of clusters with good fits beyond the current gold sample.

This work has found evidence for the existence of black holes in certain globular clusters, but makes no estimates about the expected number or mass distribution of black holes within the clusters. Further analysis of the rates at which high-velocity stars are ejected from different interactions could provide a lower limit on the number and mass of black holes expected for a particular cluster.

Appendix A

Clusters Containing Candidate High-Velocity Stars: Filters

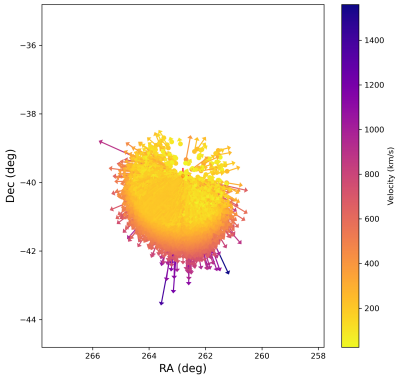

(a) The positions of the stars after the direction of motion and cluster core origin selection filters for the cluster FSR 1758. The arrows indicate the direction of motion of the stars in the plane of the sky. The plot is centered on the core of the cluster.

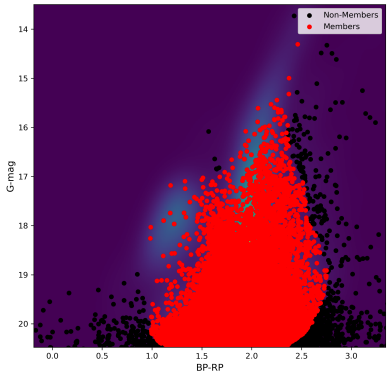

(b) A kernel density estimate plot of the CMD for this star cluster, FSR 1758. The stars identified as non-members are shown as black points, while those in red are possible cluster members according to their position on the CMD.

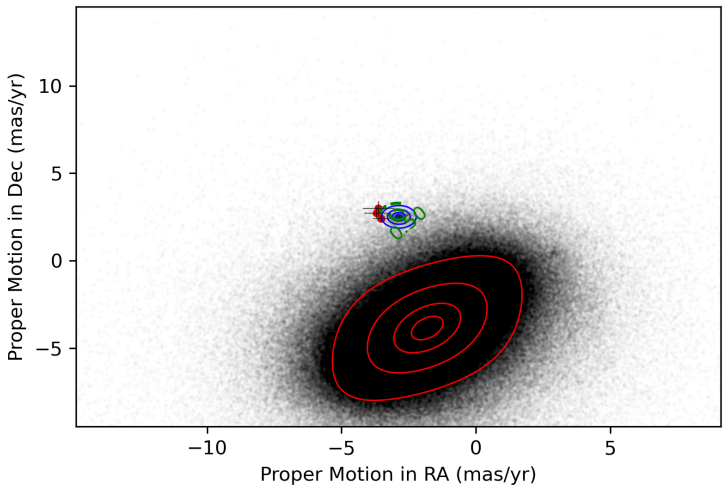

(c) The cluster FSR 1758 is the central overdensity of stars in proper-motion space, with the fit to its proper-motion distribution represented by the blue contours. The red contours represent the fitted contaminant population for this cluster, while the green dashed contours are a representation of where a star might be equally likely to be a cluster star or contaminant star, 80% likely to belong the cluster, and 95% likely to belong to the cluster, calculated using the probability procedure from Section 2.3. The high-velocity candidates found for this cluster are in red, with the errors on the proper motion measurements represented by the faint grey lines.

Figure A.1: Results of the filters in Chapter 2 for the cluster FSR 1758.

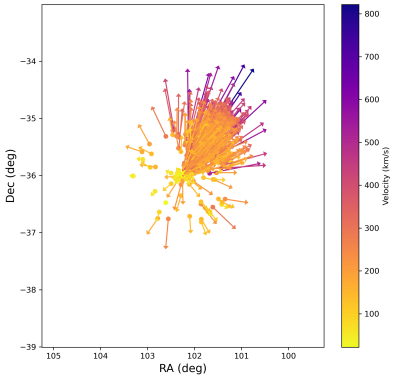

(a) The positions of the stars after the direction of motion and cluster core origin selection filters for the cluster NGC 2298. The arrows indicate the direction of motion of the stars in the plane of the sky. The plot is centered on the core of the cluster.

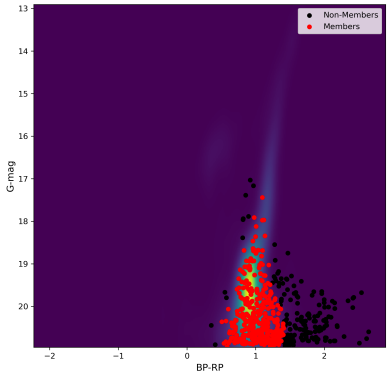

(b) A kernel density estimate plot of the CMD for this star cluster, NGC 2298. The stars identified as non-members are shown as black points, while those in red are possible cluster members according to their position on the CMD.

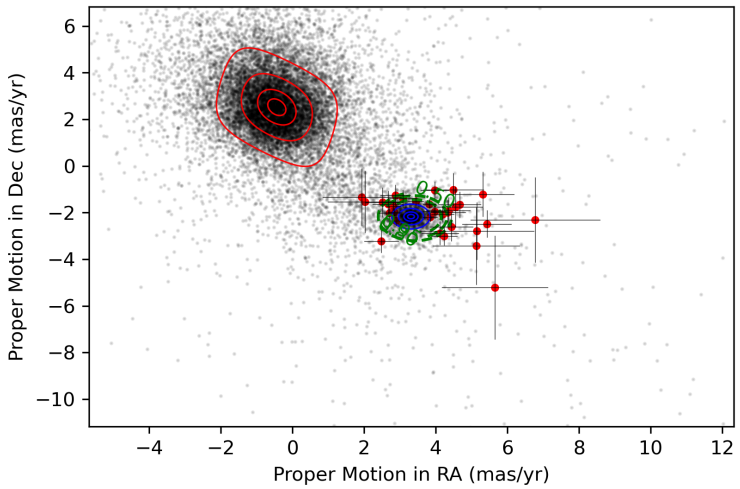

(c) The cluster NGC 2298 is the central overdensity of stars in proper-motion space, with the fit to its proper-motion distribution represented by the blue contours. The red contours represent the fitted contaminant population for this cluster, while the green dashed contours are a representation of where a star might be equally likely to be a cluster star or contaminant star, 80% likely to belong the cluster, and 95% likely to belong to the cluster, calculated using the probability procedure from Section 2.3. The high-velocity candidates found for this cluster are in red, with the errors on the proper motion measurements represented by the faint grey lines.

Figure A.2: Results of the filters in Chapter 2 for the cluster NGC 2298.

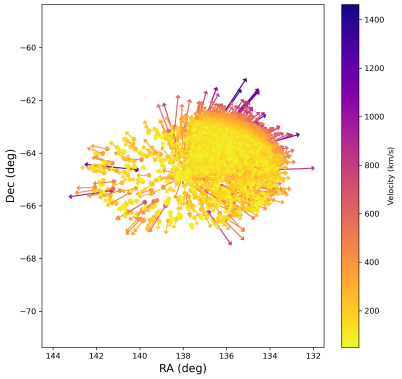

(a) The positions of the stars after the direction of motion and cluster core origin selection filters for the cluster NGC 2808. The arrows indicate the direction of motion of the stars in the plane of the sky. The plot is centered on the core of the cluster.

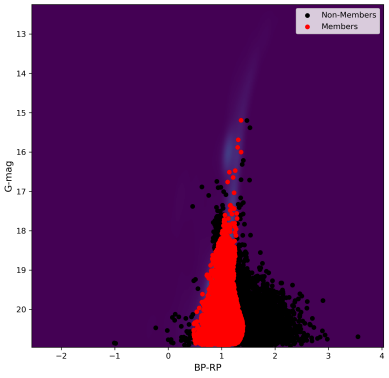

(b) A kernel density estimate plot of the CMD for this star cluster, NGC 2808. The stars identified as non-members are shown as black points, while those in red are possible cluster members according to their position on the CMD.

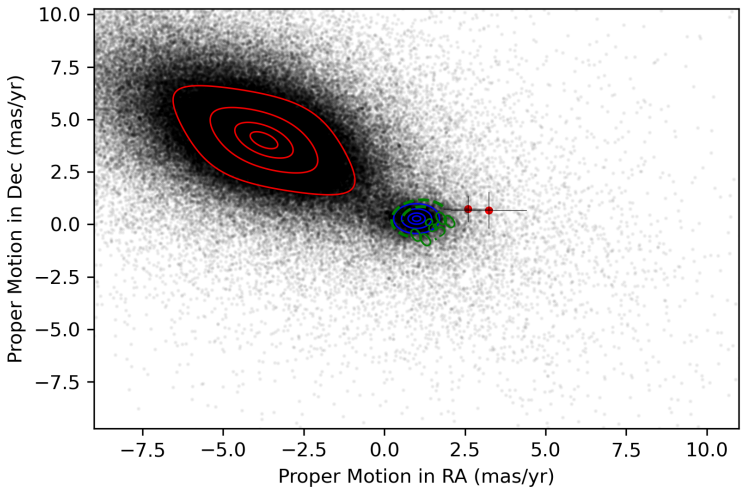

(c) The cluster NGC 2808 is the central overdensity of stars in proper-motion space, with the fit to its proper-motion distribution represented by the blue contours. The red contours represent the fitted contaminant population for this cluster, while the green dashed contours are a representation of where a star might be equally likely to be a cluster star or contaminant star (50%), 80% likely to belong the cluster, and 95% likely to belong to the cluster, calculated using the probability procedure from Section 2.3. The high-velocity candidates found for this cluster are in red, with the errors on the proper motion measurements represented by the faint grey lines.

Figure A.3: Results of the filters in Chapter 2 for the cluster NGC 2808.

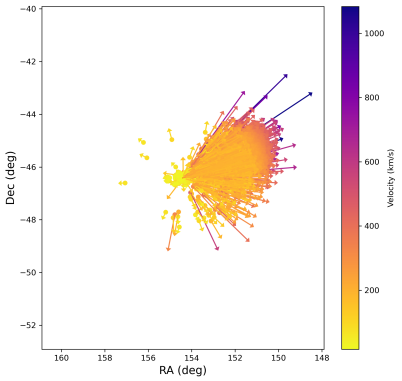

(a) The positions of the stars after the direction of motion and cluster core origin selection filters for the cluster NGC 3201. The arrows indicate the direction of motion of the stars in the plane of the sky. The plot is centered on the core of the cluster.

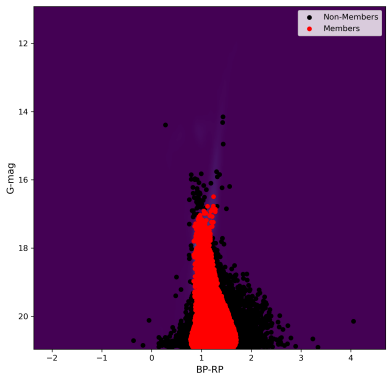

(b) A kernel density estimate plot of the CMD for this star cluster, NGC 3201. The stars identified as non-members are shown as black points, while those in red are possible cluster members according to their position on the CMD.

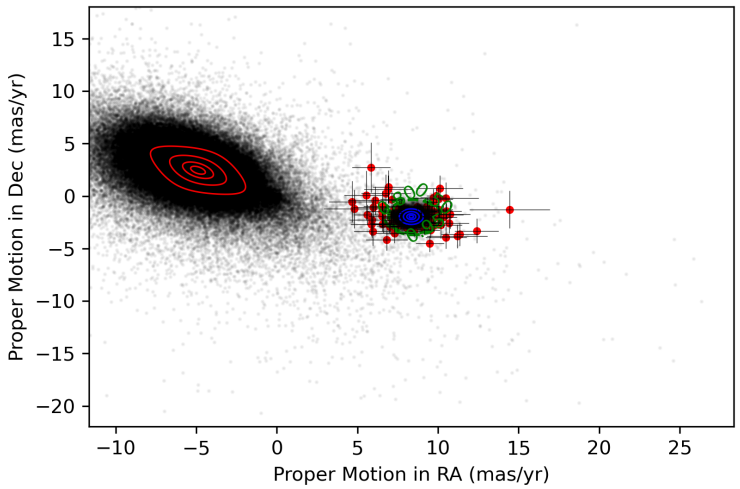

(c) The cluster NGC 3201 is the central overdensity of stars in proper-motion space, with the fit to its proper-motion distribution represented by the blue contours. The red contours represent the fitted contaminant population for this cluster, while the green dashed contours are a representation of where a star might be equally likely to be a cluster star or contaminant star, 80% likely to belong the cluster, and 95% likely to belong to the cluster, calculated using the probability procedure from Section 2.3. The high-velocity candidates found for this cluster are in red, with the errors on the proper motion measurements represented by the faint grey lines.

Figure A.4: Results of the filters in Chapter 2 for the cluster NGC 3201.

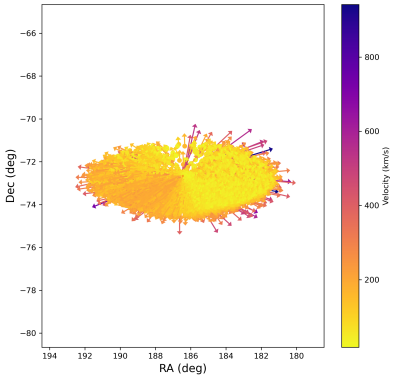

(a) The positions of the stars after the direction of motion and cluster core origin selection filters for the cluster NGC 4372. The arrows indicate the direction of motion of the stars in the plane of the sky. The plot is centered on the core of the cluster.

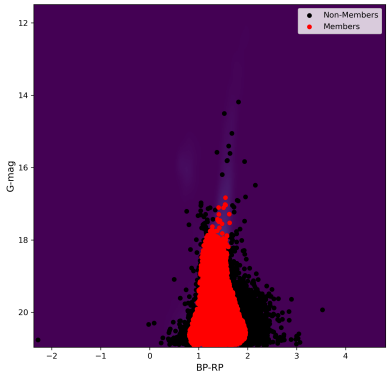

(b) A kernel density estimate plot of the CMD for this star cluster, NGC 4372. The stars identified as non-members are shown as black points, while those in red are possible cluster members according to their position on the CMD.

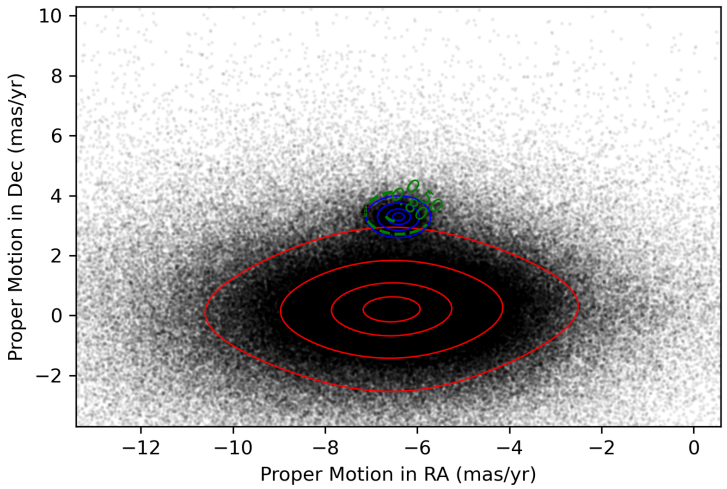

(c) The cluster NGC 4372 is the central overdensity of stars in proper-motion space, with the fit to its proper-motion distribution represented by the blue contours. The red contours represent the fitted contaminant population for this cluster, while the green dashed contours are a representation of where a star might be equally likely to be a cluster star or contaminant star, 80% likely to belong the cluster, and 95% likely to belong to the cluster, calculated using the probability procedure from Section 2.3. The high-velocity candidates found for this cluster are in red, with the errors on the proper motion measurements represented by the faint grey lines.

Figure A.5: Results of the filters in Chapter 2 for the cluster NGC 4372.

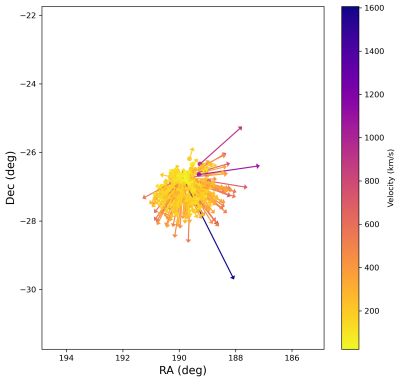

(a) The positions of the stars after the direction of motion and cluster core origin selection filters for the cluster NGC 4590. The arrows indicate the direction of motion of the stars in the plane of the sky. The plot is centered on the core of the cluster.

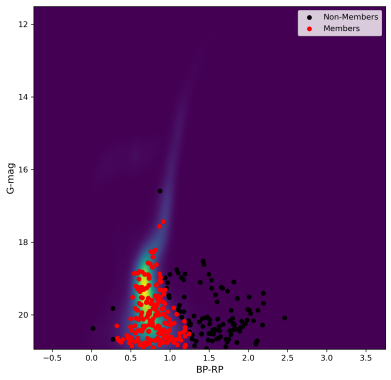

(b) A kernel density estimate plot of the CMD for this star cluster, NGC 4590. The stars identified as non-members are shown as black points, while those in red are possible cluster members according to their position on the CMD.

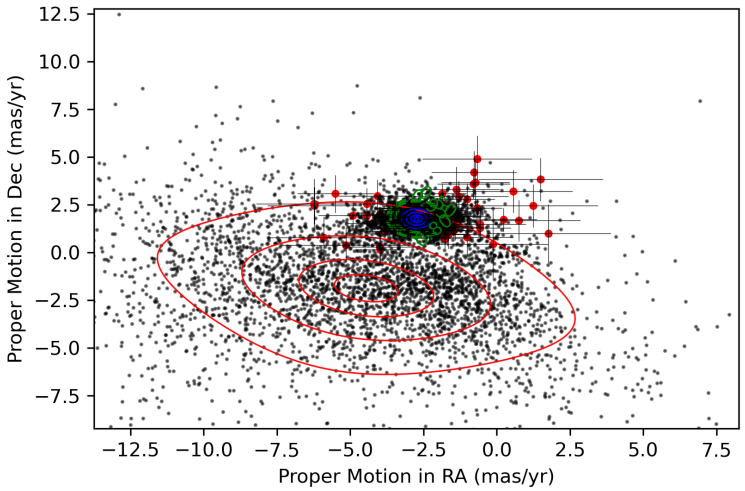

(c) The cluster NGC 4590 is the central overdensity of stars in proper-motion space, with the fit to its proper-motion distribution represented by the blue contours. The red contours represent the fitted contaminant population for this cluster, while the green dashed contours are a representation of where a star might be equally likely to be a cluster star or contaminant star, 80% likely to belong the cluster, and 95% likely to belong to the cluster, calculated using the probability procedure from Section 2.3. The high-velocity candidates found for this cluster are in red, with the errors on the proper motion measurements represented by the faint grey lines.

Figure A.6: Results of the filters in Chapter 2 for the cluster NGC 4590.

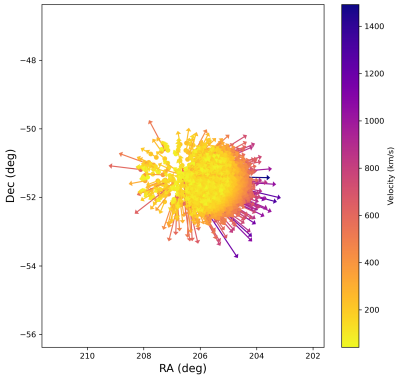

(a) The positions of the stars after the direction of motion and cluster core origin selection filters for the cluster NGC 5286. The arrows indicate the direction of motion of the stars in the plane of the sky. The plot is centered on the core of the cluster.

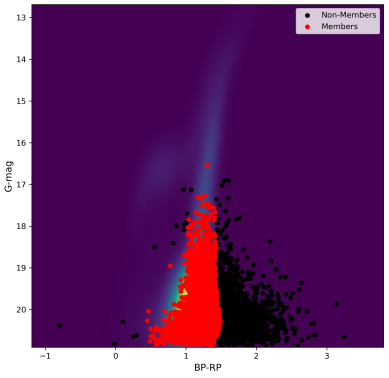

(b) A kernel density estimate plot of the CMD for this star cluster, NGC 5286. The stars identified as non-members are shown as black points, while those in red are possible cluster members according to their position on the CMD.

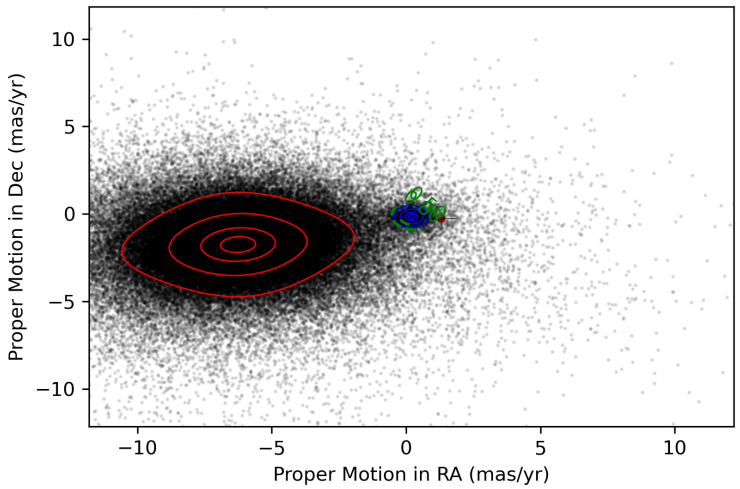

(c) The cluster NGC 5286 is the central overdensity of stars in proper-motion space, with the fit to its proper-motion distribution represented by the blue contours. The red contours represent the fitted contaminant population for this cluster, while the green dashed contours are a representation of where a star might be equally likely to be a cluster star or contaminant star, 80% likely to belong the cluster, and 95% likely to belong to the cluster, calculated using the probability procedure from Section 2.3. The high-velocity candidates found for this cluster are in red, with the errors on the proper motion measurements represented by the faint grey lines.

Figure A.7: Results of the filters in Chapter 2 for the cluster NGC 5286.

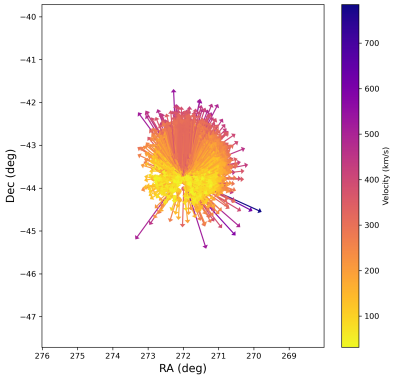

(a) The positions of the stars after the direction of motion and cluster core origin selection filters for the cluster NGC 6541. The arrows indicate the direction of motion of the stars in the plane of the sky. The plot is centered on the core of the cluster.

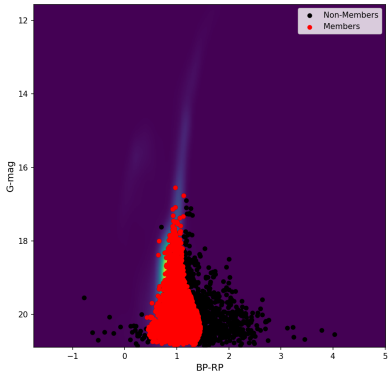

(b) A kernel density estimate plot of the CMD for this star cluster, NGC 6541. The stars identified as non-members are shown as black points, while those in red are possible cluster members according to their position on the CMD.

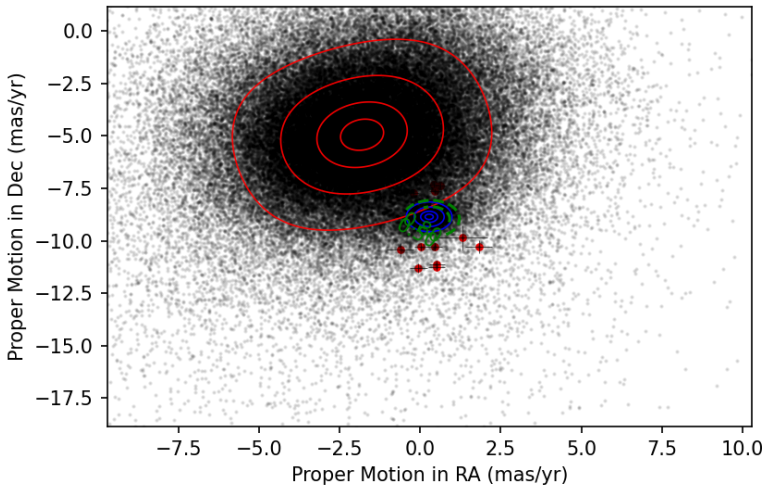

(c) The cluster NGC 6541 is the central overdensity of stars in proper-motion space, with the fit to its proper-motion distribution represented by the blue contours. The red contours represent the fitted contaminant population for this cluster, while the green dashed contours are a representation of where a star might be equally likely to be a cluster star or contaminant star, 80% likely to belong the cluster, and 95% likely to belong to the cluster, calculated using the probability procedure from Section 2.3. The high-velocity candidates found for this cluster are in red, with the errors on the proper motion measurements represented by the faint grey lines.

Figure A.8: Results of the filters in Chapter 2 for the cluster NGC 6541.

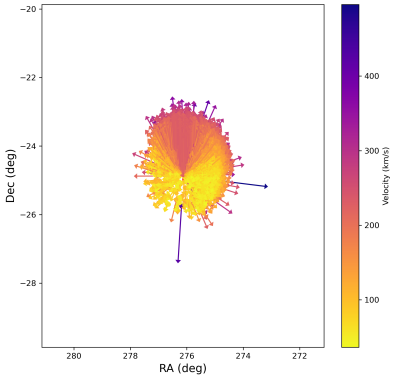

(a) The positions of the stars after the direction of motion and cluster core origin selection filters for the cluster NGC 6626. The arrows indicate the direction of motion of the stars in the plane of the sky. The plot is centered on the core of the cluster.

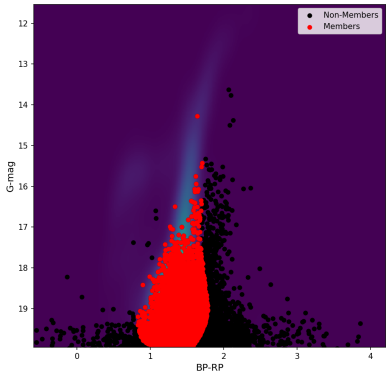

(b) A kernel density estimate plot of the CMD for this star cluster, NGC 6626. The stars identified as non-members are shown as black points, while those in red are possible cluster members according to their position on the CMD.

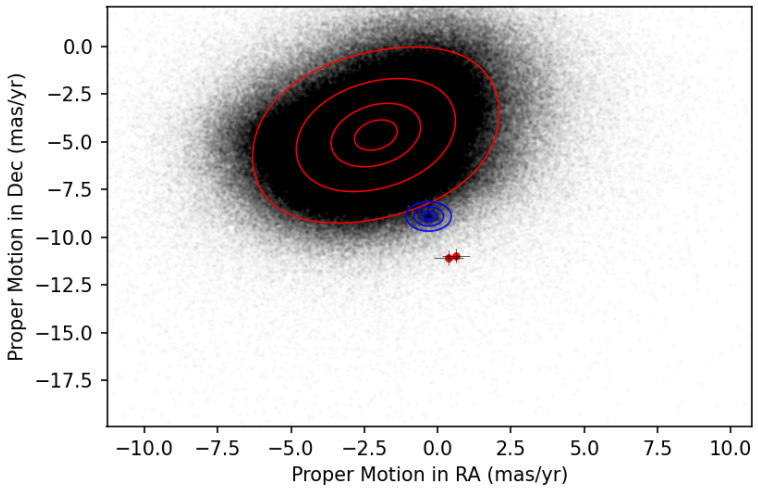

(c) The cluster NGC 6626 is the central overdensity of stars in proper-motion space, with the fit to its proper-motion distribution represented by the blue contours. The red contours represent the fitted contaminant population for this cluster, while the green dashed contours are a representation of where a star might be equally likely to be a cluster star or contaminant star, 80% likely to belong the cluster, and 95% likely to belong to the cluster, calculated using the probability procedure from Section 2.3. The high-velocity candidates found for this cluster are in red, with the errors on the proper motion measurements represented by the faint grey lines.

Figure A.9: Results of the filters in Chapter 2 for the cluster NGC 6626.

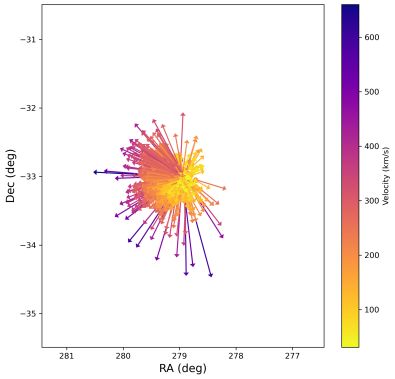

(a) The positions of the stars after the direction of motion and cluster core origin selection filters for the cluster NGC 6652. The arrows indicate the direction of motion of the stars in the plane of the sky. The plot is centered on the core of the cluster.

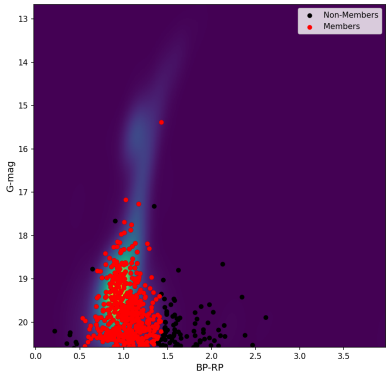

(b) A kernel density estimate plot of the CMD for this star cluster, NGC 6652. The stars identified as non-members are shown as black points, while those in red are possible cluster members according to their position on the CMD.

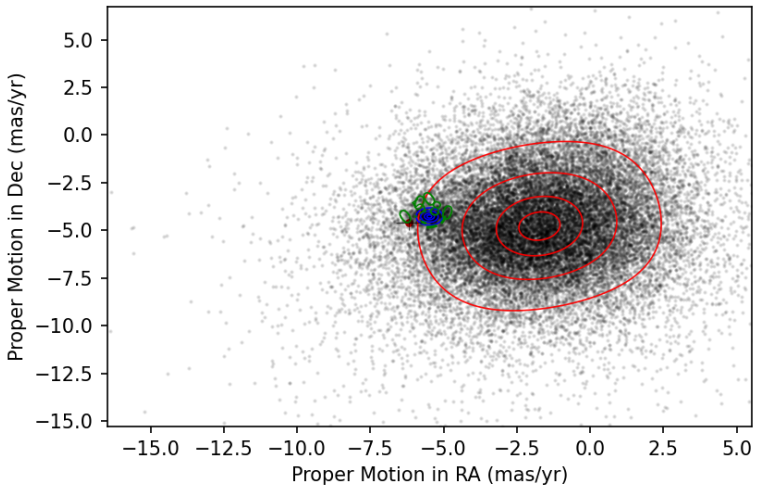

(c) The cluster NGC 6652 is the central overdensity of stars in proper-motion space, with the fit to its proper-motion distribution represented by the blue contours. The red contours represent the fitted contaminant population for this cluster, while the green dashed contours are a representation of where a star might be equally likely to be a cluster star or contaminant star, 80% likely to belong the cluster, and 95% likely to belong to the cluster, calculated using the probability procedure from Section 2.3. The high-velocity candidates found for this cluster are in red, with the errors on the proper motion measurements represented by the faint grey lines.

Figure A.10: Results of the filters in Chapter 2 for the cluster NGC 6652.

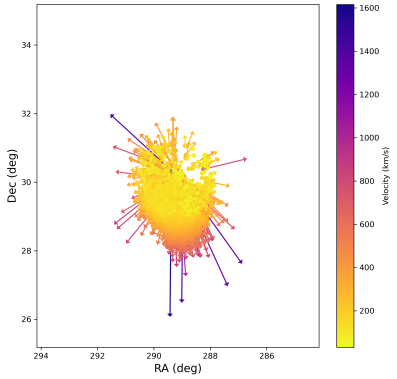

(a) The positions of the stars after the direction of motion and cluster core origin selection filters for the cluster NGC 6779. The arrows indicate the direction of motion of the stars in the plane of the sky. The plot is centered on the core of the cluster.

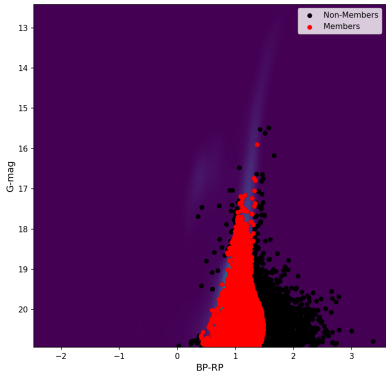

(b) A kernel density estimate plot of the CMD for this star cluster, NGC 6779. The stars identified as non-members are shown as black points, while those in red are possible cluster members according to their position on the CMD.

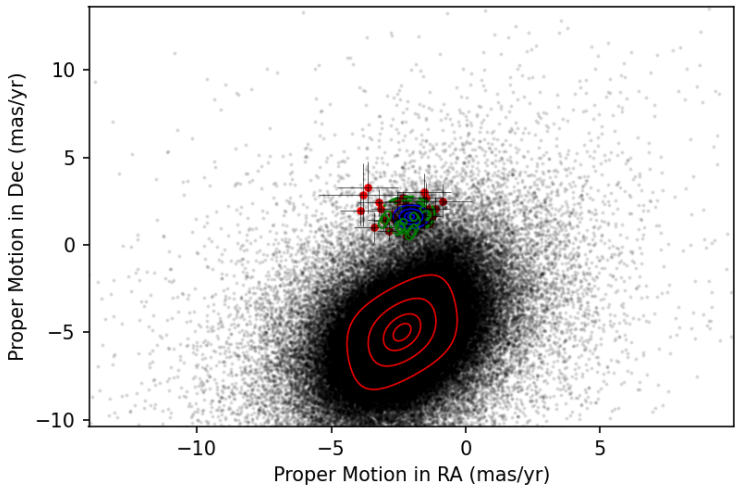

(c) The cluster NGC 6779 is the central overdensity of stars in proper-motion space, with the fit to its proper-motion distribution represented by the blue contours. The red contours represent the fitted contaminant population for this cluster, while the green dashed contours are a representation of where a star might be equally likely to be a cluster star or contaminant star, 80% likely to belong the cluster, and 95% likely to belong to the cluster, calculated using the probability procedure from Section 2.3. The high-velocity candidates found for this cluster are in red, with the errors on the proper motion measurements represented by the faint grey lines.

Figure A.11: Results of the filters in Chapter 2 for the cluster NGC 6779.

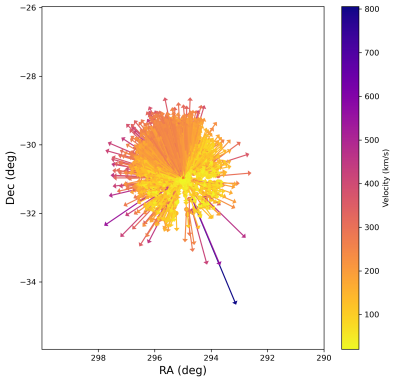

(a) The positions of the stars after the direction of motion and cluster core origin selection filters for the cluster NGC 6809. The arrows indicate the direction of motion of the stars in the plane of the sky. The plot is centered on the core of the cluster.

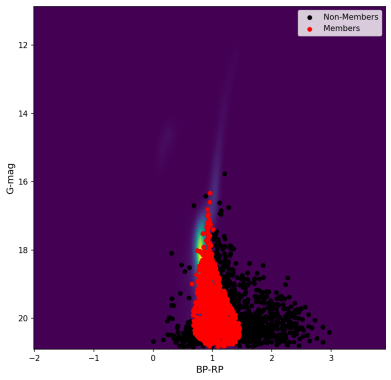

(b) A kernel density estimate plot of the CMD for this star cluster, NGC 6809. The stars identified as non-members are shown as black points, while those in red are possible cluster members according to their position on the CMD.

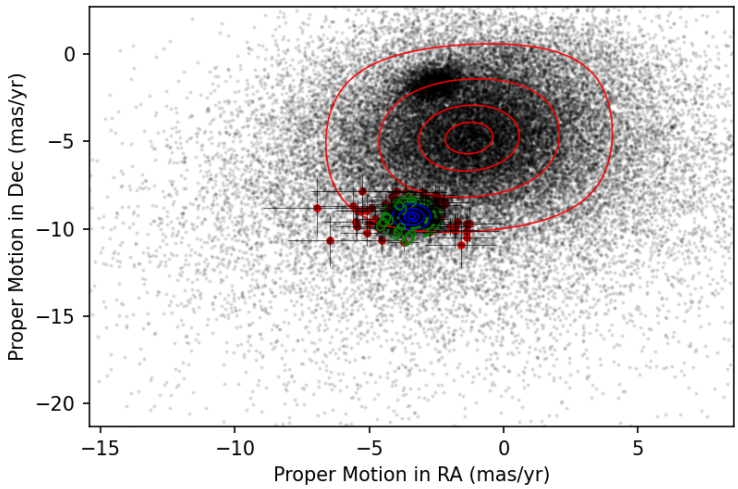

(c) The cluster NGC 6809 is the central overdensity of stars in proper-motion space, with the fit to its proper-motion distribution represented by the blue contours. The red contours represent the fitted contaminant population for this cluster, while the green dashed contours are a representation of where a star might be equally likely to be a cluster star or contaminant star, 80% likely to belong the cluster, and 95% likely to belong to the cluster, calculated using the probability procedure from Section 2.3. The high-velocity candidates found for this cluster are in red, with the errors on the proper motion measurements represented by the faint grey lines.

Figure A.12: Results of the filters in Chapter 2 for the cluster NGC 6809.

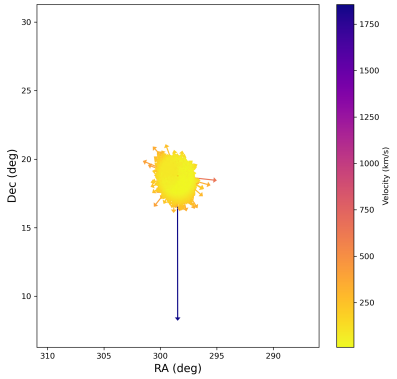

(a) The positions of the stars after the direction of motion and cluster core origin selection filters for the cluster NGC 6838. The arrows indicate the direction of motion of the stars in the plane of the sky. The plot is centered on the core of the cluster.

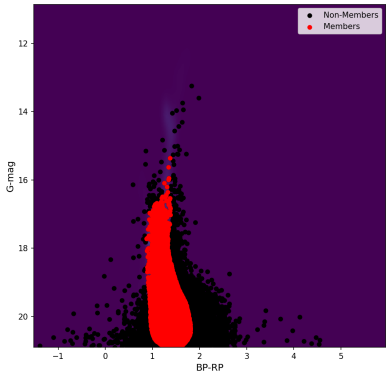

(b) A kernel density estimate plot of the CMD for this star cluster, NGC 6838. The stars identified as non-members are shown as black points, while those in red are possible cluster members according to their position on the CMD.

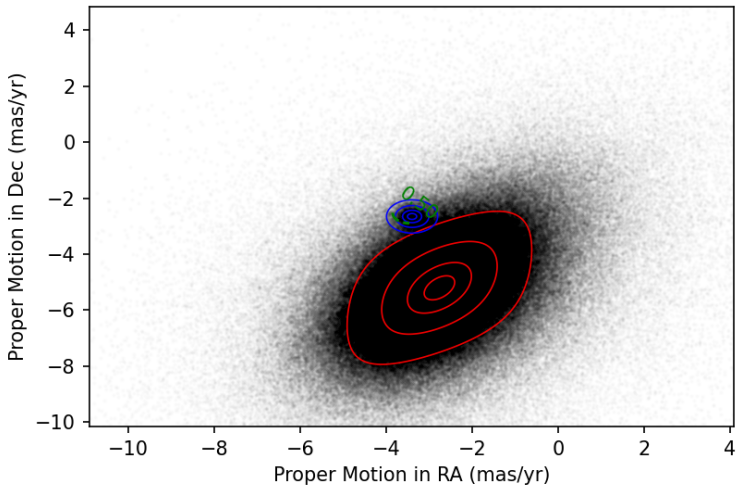

(c) The cluster NGC 6838 is the central overdensity of stars in proper-motion space, with the fit to its proper-motion distribution represented by the blue contours. The red contours represent the fitted contaminant population for this cluster, while the green dashed contours are a representation of where a star might be equally likely to be a cluster star or contaminant star, 80% likely to belong the cluster, and 95% likely to belong to the cluster, calculated using the probability procedure from Section 2.3. The high-velocity candidates found for this cluster are in red, with the errors on the proper motion measurements represented by the faint grey lines.

Figure A.13: Results of the filters in Chapter 2 for the cluster NGC 6838.

Appendix B

Clusters Containing Candidate High-Velocity Stars: Results

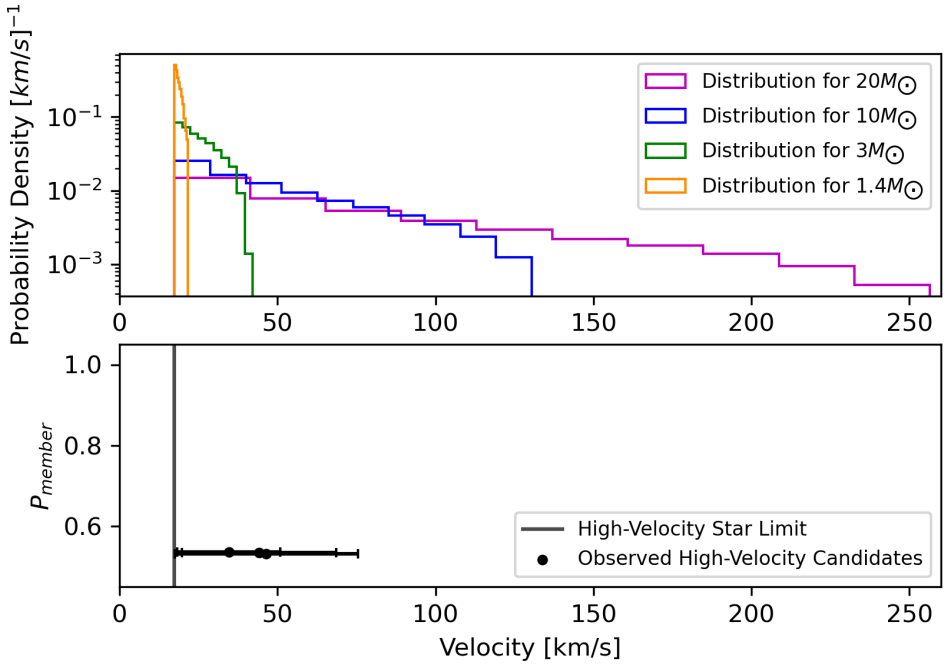

Figure B.1: The velocity of the observed high-velocity star candidates, compared to the analytic velocity distribution for a range of binary masses, for the cluster FSR 1758. The distributions in the upper panel begin at the lower velocity threshold for a high-velocity star. These distributions are indicated by the coloured lines if sufficient stars are produced at a high velocity, or by a vertical line (indicating the theoretical maximum ejection velocity for a given interaction) if very few high-velocity stars are produced for a given interaction. The high-velocity star candidates for the cluster are displayed in the bottom panel, with their cluster membership probability on the y-axis.

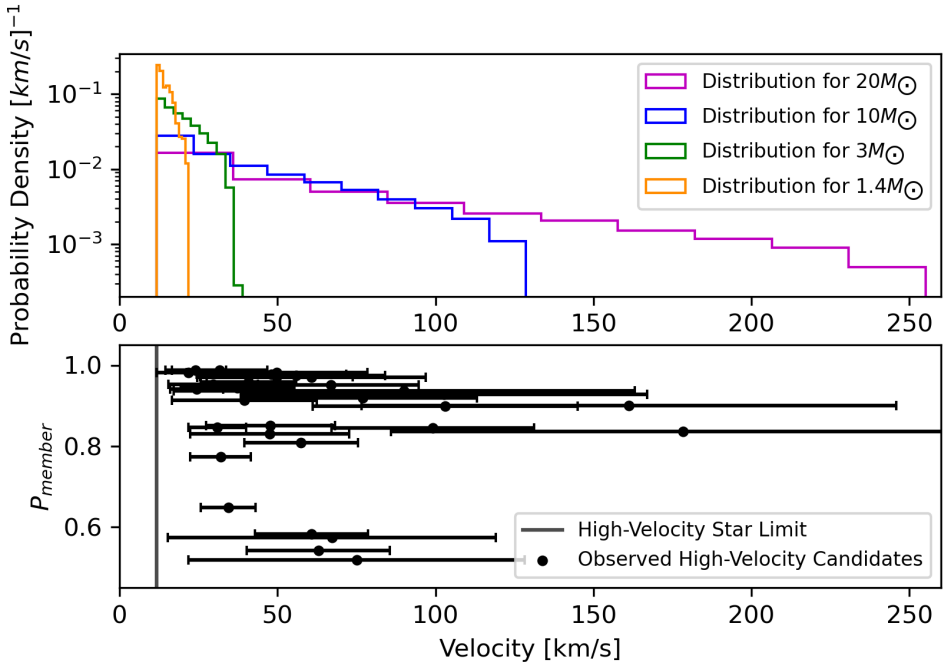

Figure B.2: Same plot as Figure B.1, for NGC 2298.

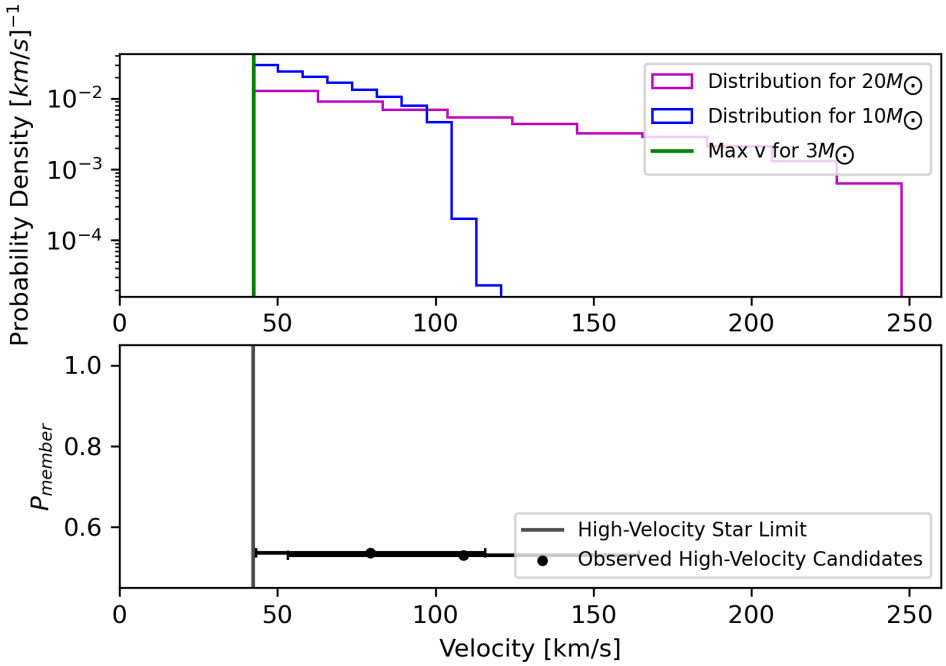

Figure B.3: Same plot as Figure B.1, for NGC 2808.

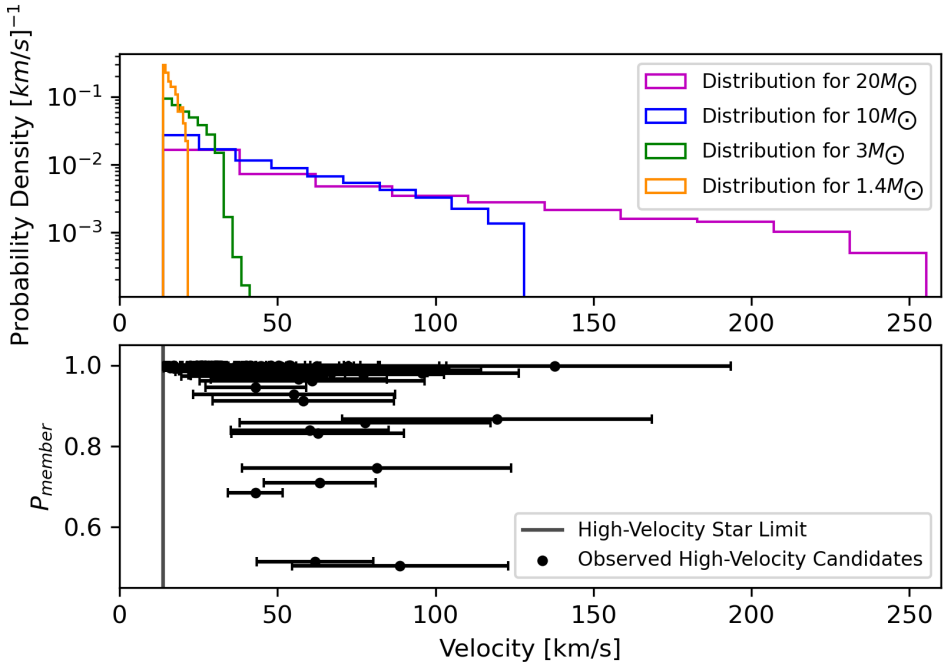

Figure B.4: Same plot as Figure B.1, for NGC 3201.

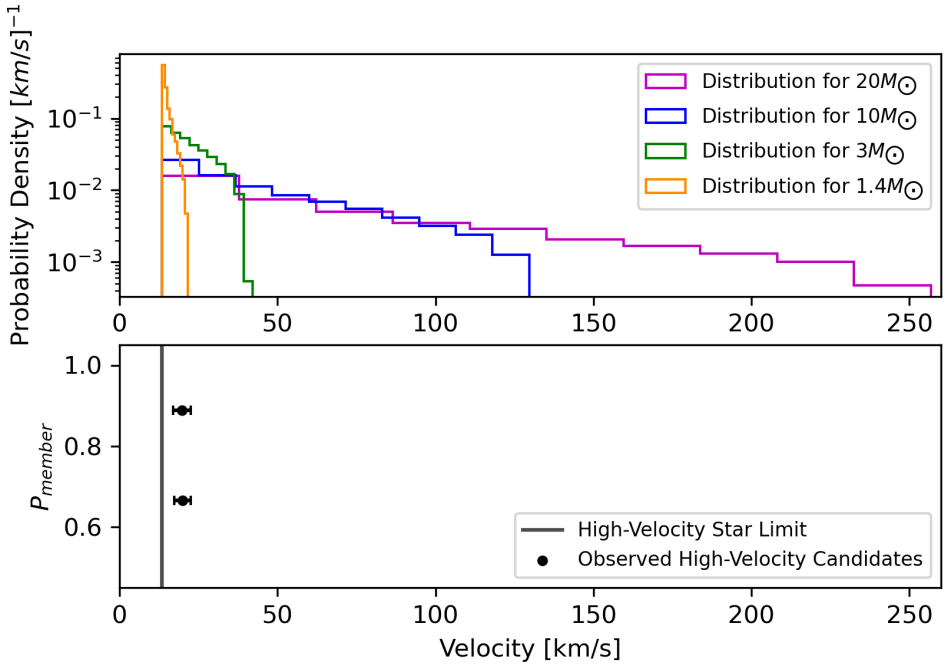

Figure B.5: Same plot as Figure B.1, for NGC 4372.

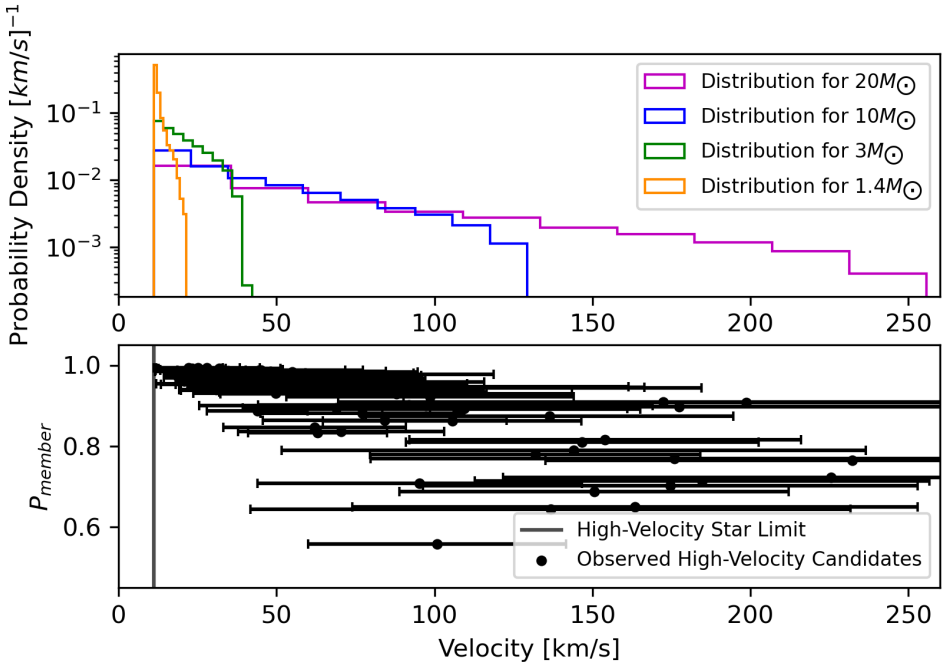

Figure B.6: Same plot as Figure B.1, for NGC 4590.

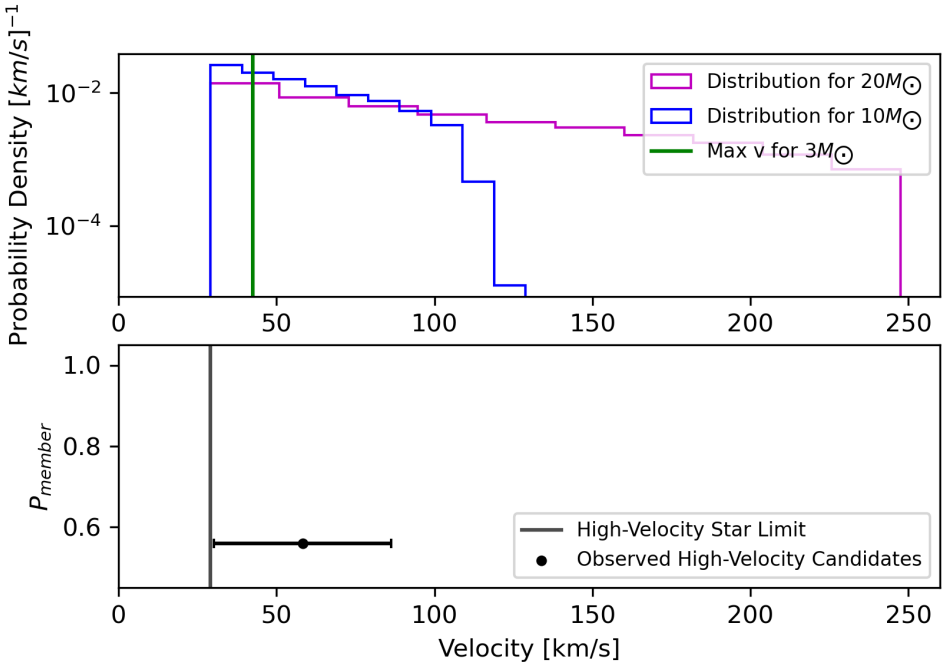

Figure B.7: Same plot as Figure B.1, for NGC 5286.

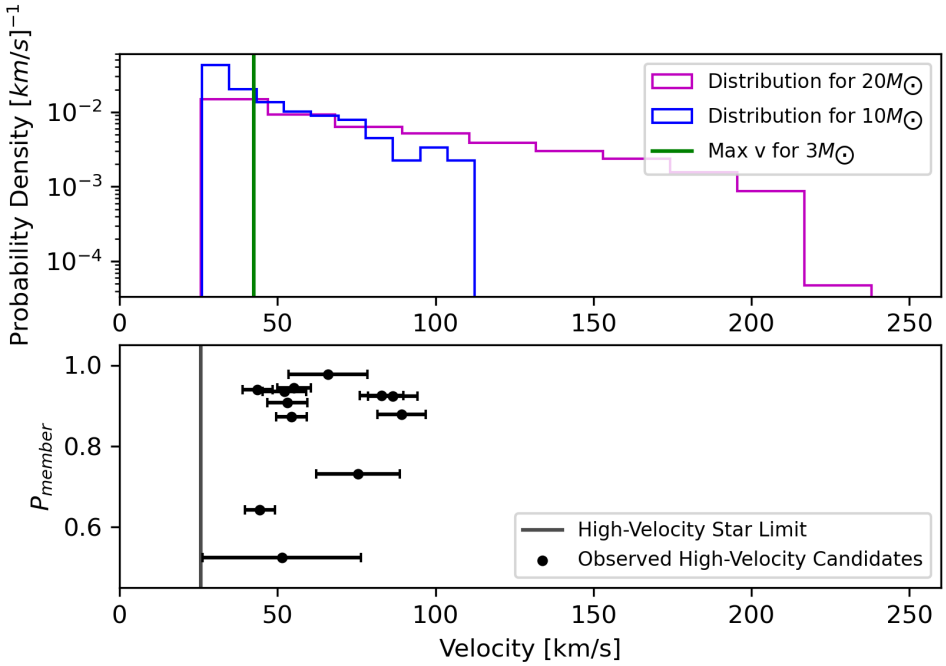

Figure B.8: Same plot as Figure B.1, for NGC 6541.

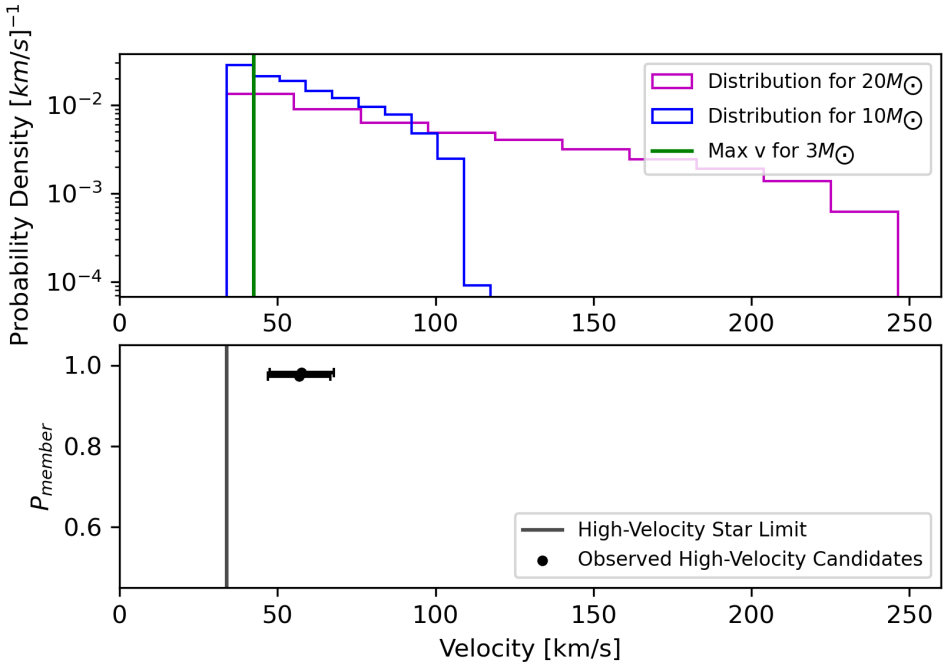

Figure B.9: Same plot as Figure B.1, for NGC 6626.

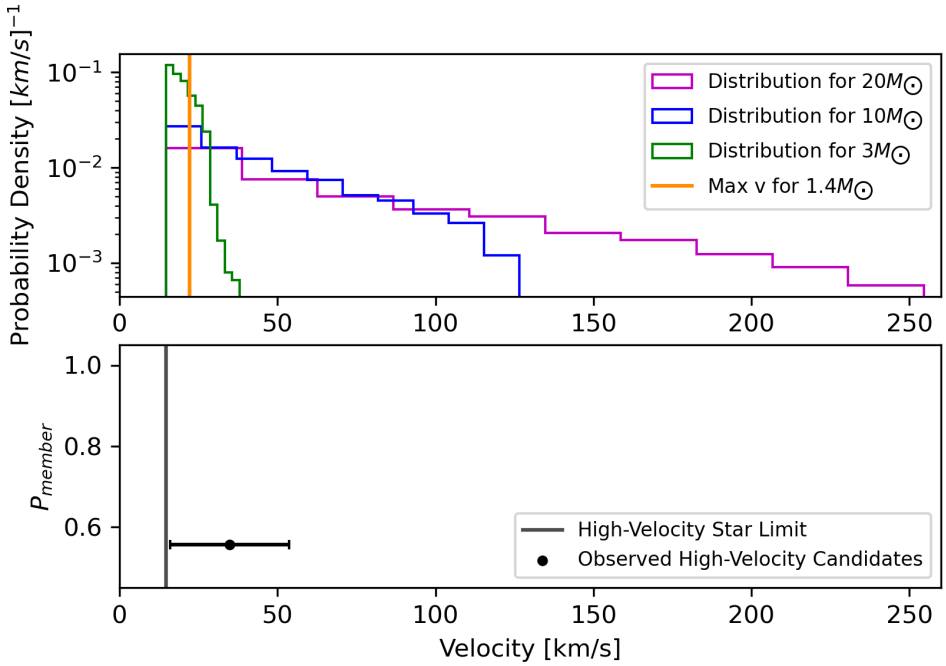

Figure B.10: Same plot as Figure B.1, for NGC 6652.

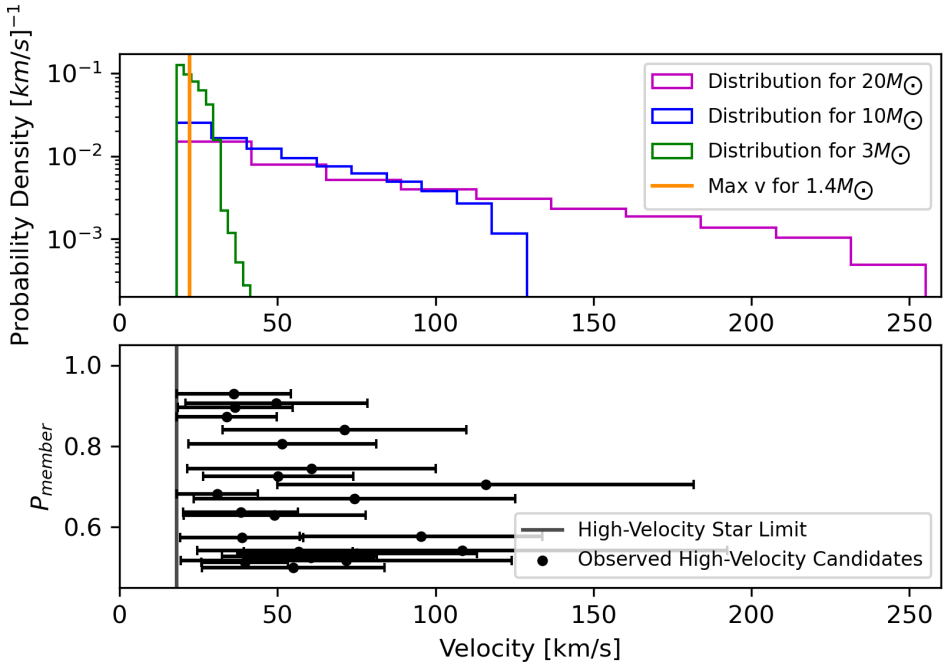

Figure B.11: Same plot as Figure B.1, for NGC 6779.

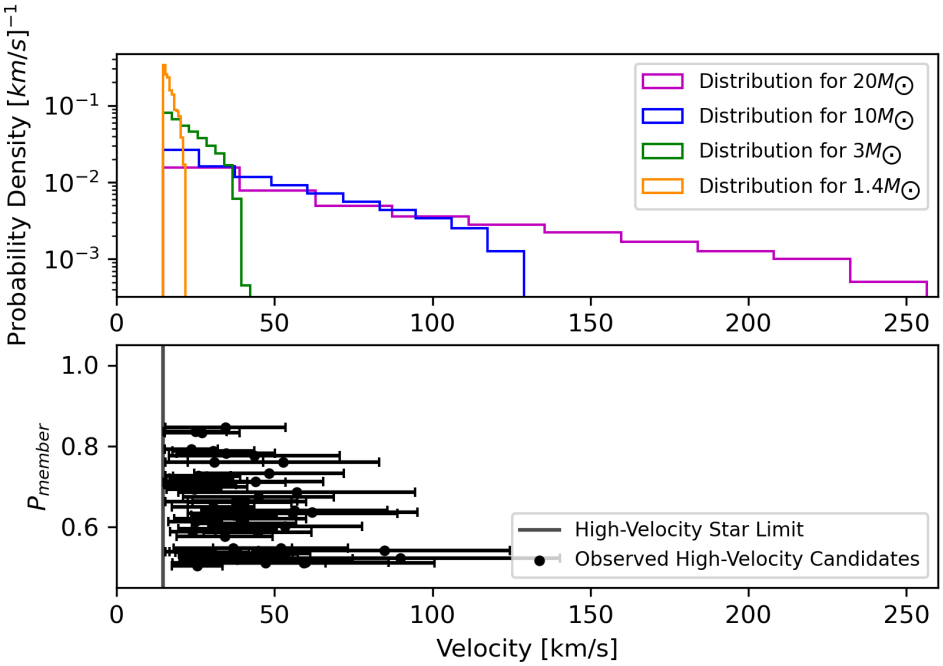

Figure B.12: Same plot as Figure B.1, for NGC 6809.

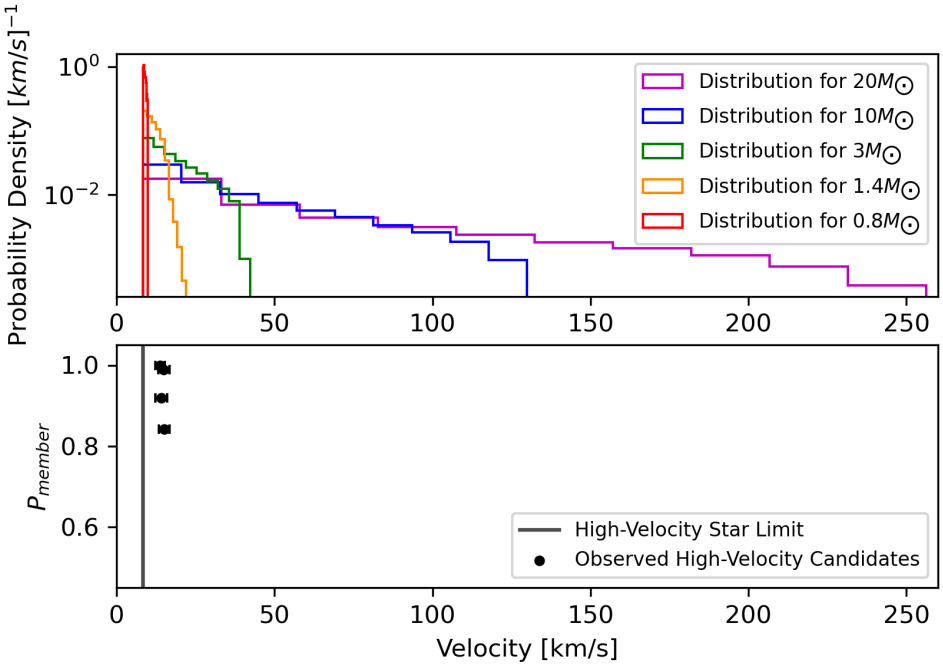

Figure B.13: Same plot as Figure B.1, for NGC 6838.

Appendix C

Acknowledgements

This work has made use of data from the European Space Agency (ESA) mission *Gaia* (`https://www.cosmos.esa.int/gaia`), processed by the *Gaia* Data Processing and Analysis Consortium (DPAC, `https://www.cosmos.esa.int/web/gaia/dpac/consortium`). Funding for the DPAC has been provided by national institutions, in particular the institutions participating in the *Gaia* Multilateral Agreement.

Bibliography

Abbott B. P., et al., 2016, Physical Review Letters, 116, 131103

Antonini F., Rasio F. A., 2016, Astrophysical Journal, 831, 187

Antonini F., Gieles M., Gualandris A., 2019, Monthly Notices of the Royal Astronomical Society, 486, 5008

Askar A., Arca Sedda M., Giersz M., 2018, Monthly Notices of the Royal Astronomical Society, 478, 1844

Baumgardt H., 2017, Monthly Notices of the Royal Astronomical Society, 464, 2174

Baumgardt H., Hilker M., 2018, Monthly Notices of the Royal Astronomical Society, 478, 1520

Cabrera T., Rodriguez C. L., 2023, arXiv e-prints, p. arXiv:2302.03048

Dejonghe H., 1987, Monthly Notices of the Royal Astronomical Society, 224, 13

Dickson N., 2022, Master's thesis, Saint Mary's University

Feroz F., Hobson M. P., Bridges M., 2009, Monthly Notices of the Royal Astronomical Society, 398, 1601

Fragione G., Gualandris A., 2019, Monthly Notices of the Royal Astronomical Society, 489, 4543

Gaia Collaboration et al., 2016, Astronomy and Astrophysics, 595, A1

Gaia Collaboration et al., 2022a, arXiv e-prints, p. arXiv:2206.06207

Gaia Collaboration et al., 2022b, arXiv e-prints, p. arXiv:2208.00211

Giersz M., Leigh N., Hypki A., Lützgendorf N., Askar A., 2015, Monthly Notices of the Royal Astronomical Society, 454, 3150

Gvaramadze V. V., Gualandris A., Portegies Zwart S., 2009, Monthly Notices of the Royal Astronomical Society, 396, 570

Habets G. M. H. J., Heintze J. R. W., 1981, Astronomy and Astrophysics, Supplement, 46, 193

Handley W. J., Hobson M. P., Lasenby A. N., 2015a, Monthly Notices of the Royal Astronomical Society, 450, L61

Handley W. J., Hobson M. P., Lasenby A. N., 2015b, Monthly Notices of the Royal Astronomical Society, 453, 4384

Harris W. E., 2010, arXiv e-prints, p. arXiv:1012.3224

Heggie D., Hut P., 2003, The Gravitational Million-Body Problem: A Multidisciplinary Approach to Star Cluster Dynamics

Hills J. G., Fullerton L. W., 1980, Astronomical Journal, 85, 1281

Hut P., et al., 1992, Publications of the ASP, 104, 981

Hut P., McMillan S., Makino J., Portegies Zwart S., 2010, Starlab: A Software Environment for Collisional Stellar Dynamics, Astrophysics Source Code Library, record ascl:1010.076 (ascl:1010.076)

Lützgendorf N., et al., 2012, Astronomy and Astrophysics, 543, A82

Mapelli M., Santoliquido F., Bouffanais Y., Arca Sedda M. A., Artale M. C., Ballone A., 2021, Symmetry, 13, 1678

Meylan G., Dubath P., Mayor M., 1991, Astrophysical Journal, 383, 587

Miller M. C., Lauburg V. M., 2009, Astrophysical Journal, 692, 917

Neal R. M., 2003, The Annals of Statistics, 31, 705

Plummer H. C., 1911, Monthly Notices of the Royal Astronomical Society, 71, 460

Rodriguez C. L., Zevin M., Amaro-Seoane P., Chatterjee S., Kremer K., Rasio F. A., Ye C. S., 2019, , 100, 043027

Skilling J., 2004, in Fischer R., Preuss R., Toussaint U. V., eds, American Institute of Physics Conference Series Vol. 735, Bayesian Inference and Maximum Entropy Methods in Science and Engineering: 24th International Workshop on Bayesian Inference and Maximum Entropy Methods in Science and Engineering. pp 395–405, doi:10.1063/1.1835238

Skilling J., 2006, Bayesian Analysis, 1, 833

Sollima A., Baumgardt H., 2017, Monthly Notices of the Royal Astronomical Society, 471, 3668

Sollima A., Baumgardt H., Hilker M., 2019, Monthly Notices of the Royal Astronomical Society, 485, 1460

Speagle J. S., 2020, Monthly Notices of the Royal Astronomical Society, 493, 3132

Spitzer L., 1987, Dynamical evolution of globular clusters

Vasiliev E., Baumgardt H., 2021a, Catalogue of stars in Milky Way globular clusters from Gaia EDR3, doi:10.5281/zenodo.4549398, `https://doi.org/10.5281/zenodo.4549398`

Vasiliev E., Baumgardt H., 2021b, Monthly Notices of the Royal Astronomical Society, 505, 5978

Vitral E., 2021, Monthly Notices of the Royal Astronomical Society, 504, 1355

Vitral E., Mamon G. A., 2021, Astronomy and Astrophysics, 646, A63

Weatherford N. C., Chatterjee S., Kremer K., Rasio F. A., 2020, Astrophysical Journal, 898, 162

Weatherford N. C., Fragione G., Kremer K., Chatterjee S., Ye C. S., Rodriguez C. L., Rasio F. A., 2021, Astrophysical Journal, Letters, 907, L25

Webb J. J., Harris W. E., Sills A., Hurley J. R., 2013, Astrophysical Journal, 764, 124